Revealing Sediment Transport Pathways and Geomorphic Change in Washover Fans by Combining Drone-Derived Digital Elevation Models and Single Grain Luminescence Data

Simon Matthias May[1] , **John Nikolaus Callow**[2] , **Dominik Brill**[1], **Dirk Hoffmeister**[1] , and **Jan-Hendrik May**[3,4]

[1]Institute of Geography, University of Cologne, Cologne, Germany, [2]School of Agriculture and Environment, The University of Western Australia, Crawley, WA, Australia, [3]School of Geography, Faculty of Science, University of Melbourne, Carlton, VIC, Australia, [4]GeoQuest Research Centre—School of Earth Atmospheric and Life Sciences, University of Wollongong, Wollongong, NSW, Australia

Abstract Chronostratigraphic investigations on coastal sedimentary records such as washover fans or beach-ridge sequences may be used to reconstruct storm chronologies on centennial to millennial time scales. However, modern analogs are pivotal in interpreting depositional processes and reducing uncertainty in evaluating the complex chronostratigraphic architecture of these landforms. Such a modern analog was provided by category 3 tropical cyclone (TC) Olwyn in 2015, which caused a significant storm surge in the Exmouth Gulf (Western Australia). Pre- and post-TC Olwyn geomorphological surveys and high-resolution drone-derived topographical data of a large washover fan document a detailed history of erosion and deposition during the event. The modern analog deposits provided an excellent opportunity to evaluate the use of luminescence-based proxies (luminescence inventories) for tracing event-related sediment source environments and understanding transport processes. Sediments deposited during Olwyn show a systematic relationship between luminescence characteristics and washover fan position. Seaward and central washover sections are indicated by well-bleached deposits due to the beach as the dominant source and/or long transport distances. Lateral washover deposits are characterized by rather local source areas and short transport distances, resulting in higher remnant ages of 70–140 a. Our data show that the combination of sediment source environments and sediment transport length across the fan represents the main control in resetting the luminescence signal and enabling reliable depositional ages to be calculated. It documents the benefit of investigating luminescence inventories when establishing chronologies from complex sedimentary records, thereby demanding a careful consideration of local processes and source areas when interpreting sedimentary TC records.

1. Introduction

Washover fans are typically generated by storm-related superelevations of the sea level exceeding the beach-foredune barrier due to barometric and wind-driven surge, wave-setup and wave runup, causing erosion of the dune, barrier overwash, and subsequent coastal inundation and sediment deposition (C. Donnelly et al., 2006; Matias et al., 2008, 2010; Sallenger, 2000). In most cases, they represent unambiguous geomorphological and depositional evidence of extratropical winter storms or tropical cyclones (TCs) (C. Donnelly et al., 2006; Matias et al., 2008, 2010). In contrast to instrumental or historical records, coastal sedimentary landforms and deposits such as washover fans and beach-ridge sequences may enable the reconstruction of storm frequency-magnitude patterns over centennial to millennial time scales (i.e., within the framework of palaeotempestological studies), and they potentially provide significant insights into the depositional processes and hydrodynamic conditions during these extreme-wave events (e.g., C. Donnelly et al., 2006; Forsyth et al., 2010; Lazarus & Armstrong, 2015; McCall et al., 2010; Morton & Sallenger, 2003; Nott, 2011; Nott et al., 2009; Priestas & Fagherazzi, 2010; Schwartz, 1982; Shaw et al., 2015; Tamura et al., 2019; White & Wang, 2003).

The interpretation of these sedimentary records relies on both a thorough understanding of the stratigraphical evidence and the establishment of robust chronologies. However, in highly dynamic coastal settings with constant sediment reworking, radiocarbon chronologies may be biased by chronological inaccuracies due to

reworking of marine organisms and the marine reservoir effect, and particularly in semiarid to arid climates suitable datable material is often absent. To surpass these limitations, optically stimulated luminescence (OSL) dating (e.g., Brill, Klasen, Brückner, Jankaew, Kelletat, et al., 2012; Brill, Klasen, Brückner, Jankaew, Scheffers, et al., 2012; Davids et al., 2010; Kunz et al., 2010; May et al., 2015) has been used within the framework of detailed stratigraphic, geomorphic, and chronological investigations on washover fans at Point Lefroy in Exmouth Gulf (Western Australia [WA]). The washover fans consist of an up to 2 m-thick sequence of sand, shell debris, and coral rubble alternating with intermittent palaeosols (Brill et al., 2017, 2018; Callow et al., 2018; May et al., 2017). These previous studies established a model for washover fan evolution, clearly (i) showing that depositional activity shifted across individual washover fans during the past millennia and (ii) suggesting periods of increased storm-induced deposition at ∼170, ∼360, ∼850, and ∼1,300 years ago, with further older units dated to ∼1,950, ∼2,300, and ∼2,850 years ago. Correlation with El Niño-Southern Oscillation (ENSO) proxies point to a causal link of TC occurrence and ENSO in the northern part of WA. The value and accuracy of these washover-derived (and potentially other) palaeotempestological records, however, hinge upon the completeness of the sedimentary archive it is derived from and thus require a detailed understanding of the spatio-temporal pattern of both erosive and depositional processes active on the fan during TC-induced flood events. In addition, the short and turbulent transport conditions of high-magnitude flooding events often limits the potential for completely zeroing the OSL dosimeter during sediment transport (i.e., incomplete OSL signal resetting), resulting in additional challenges when establishing highly accurate luminescence-based chronologies that are crucial in identifying event-based deposits.

In this context, recent advances in luminescence techniques have provided novel tools toward an improved understanding of event-based sediment transport processes and allow tracing sediment source environments across depositional systems (e.g., Brill et al., 2018; Gray et al., 2019). Evaluating and verifying the relationship between these sedimentary processes and (i) the dynamically changing fan-wide morpho-stratigraphy and (ii) the resulting luminescence characteristics and chronologies, however, is only possible through investigating modern events as analogs for washover fan sedimentary dynamics during an overwash event. Such a rare modern analog was provided by category 3 TC Olwyn in 2015, which crossed the NW Cape in southern direction, that is, just west of the Exmouth Gulf (e.g., May et al., 2018). TC Olwyn caused a significant storm surge along the coastlines of the Exmouth Gulf, which considerably impacted the washover fans at Point Lefroy. Significantly, this followed an intensive field campaign and collection of high-resolution data in 2014 (Brill et al., 2017, 2018; Callow et al., 2018; May et al., 2017). Therefore, TC Olwyn presented a unique opportunity to combine the high-resolution (centimeter-scale) orthophoto and topographical data from before and after the TC.

Against this background, this study presents results from post-TC Olwyn surveys carried out in 2016 and 2018, which aimed at documenting the geomorphological and sedimentary impact of TC Olwyn at the washover site, thereby testing the previously established model of washover fan evolution. Our study is based on kite (2016) and unmanned aerial vehicle (UAV, in 2014 and 2018) surveys and digital photogrammetry (Structure-from-Motion, SfM) techniques, geomorphological and sedimentological data, luminescence dating, and a suite of luminescence-based proxies for sediment dynamics (luminescence inventories) including quartz single grain age distributions and the associated remnant ages, as well as quartz and feldspar luminescence signal comparisons. It particularly aims at (i) documenting the depositional and erosional pattern of TC Olwyn; (ii) tracing sediment source environments and understanding sediment transport processes; and, ultimately, (iii) determining the accuracy of luminescence dating.

2. Regional Setting

2.1. Climatic, Geologic, and Geomorphologic Setting

The Exmouth Gulf is bordered by the NNE-SSW striking Cape Range anticline of the NW Cape (also Cape Range Peninsula) to the west (Figure 1a). Two minor parallel-striking anticline structures (Rough and Giralia Ranges) stretch toward the southern Gulf coast, with the study area located at the northern end of the Rough Range, which forms a SSW-NNE-oriented headland between the Bay of Rest and Point Lefroy (SW Exmouth Gulf). At the coast, alluvial and colluvial deposits of varying composition are covered by late Pleistocene and Holocene dune and beach deposits (Collins et al., 2003; Scheffers et al., 2008; Wyrwoll et al., 1993). Postglacial relative sea level had reached a highstand of 1–2 m above present (Lewis et al., 2013)
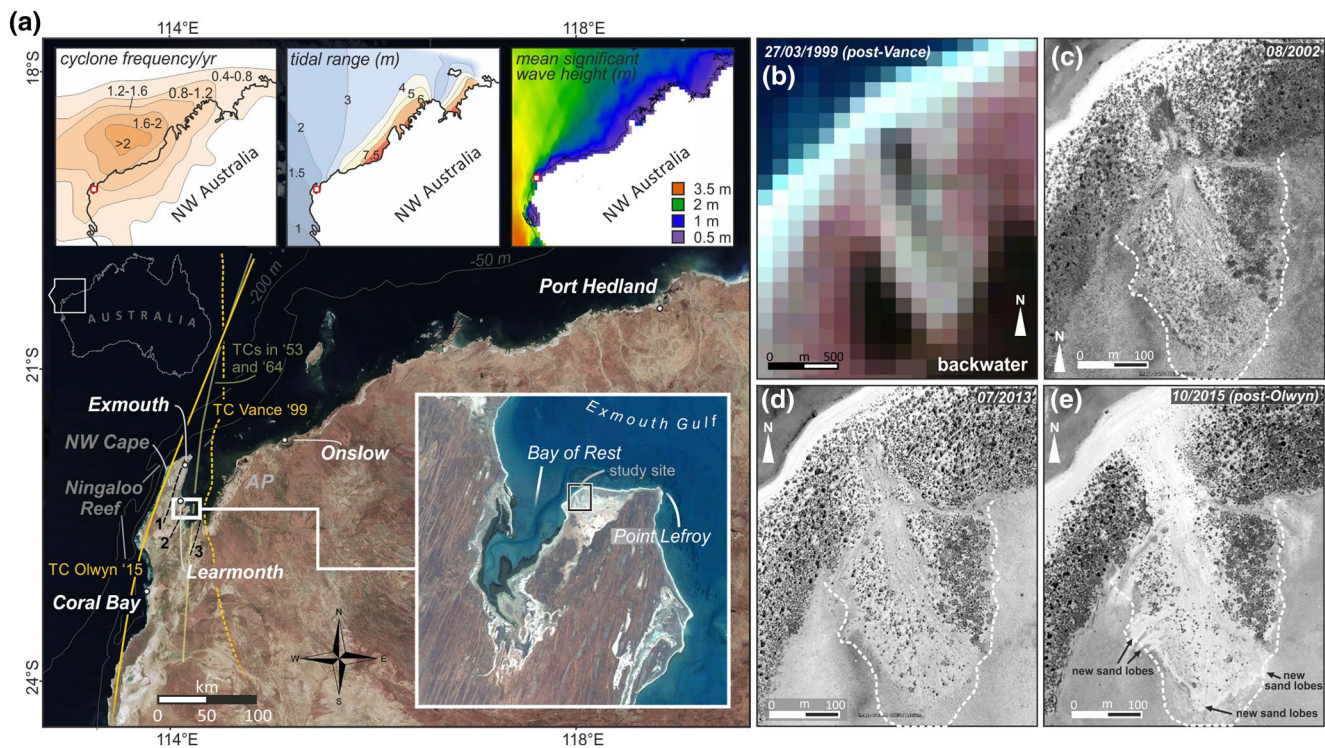
Figure 1. (a) Overview of the study area in the north-western part of Western Australia (based on data from NASA Worldview [NASA EOSDIS], Landsat satellite data [RGB 3/2/1; USGS] and SRTM data [USGS]) including cyclone frequency, tidal range (Short & Woodroffe, 2009), and wave climate (mean significant wave height, July average), which is based on the ESA GlobWave Project data (Navy Meteorology and Oceanography [METOC], Department of Defence, Australian Government). Tracks of TCs in 1953 and 1964 (approximate), TC Vance (1999), and TC Olwyn (2015) are depicted (JTWC, 2016). The study area is marked by a white frame and magnified in the inset. The washover fan investigated in this study is located between the Bay of Rest and Point Lefroy (b–e). (b) Detail of post-TC Vance Landsat satellite image from 27 March 1999 (USGS), showing backwaters in the mudflat and the central channel. The image suggests bare sediment without vegetation cover (= fresh sediment, light brown to gray/white) especially in the SW part of the fan, which is in contrast to the E fan shoulder (red colors, indicating vegetation cover) See May et al. (2017) for comparison of pre- and post-Vance images. (c–e) Google Earth images from August 2002, July 2013, and October 2015 (post-TC Olwyn) (Google Earth/Digital Globe). 1, Cape Range anticline; 2, Rough Range anticline; 3, Giralia Range anticline; AP, Ashburton Plain.

between 7,000 and 6,000 a BP and was followed by a phase of marine regression since then (Lambeck & Nakada, 1990; Lewis et al., 2013). The mean tidal range in the Gulf increases southwards from 2.1 m at Learmonth to 2.6 m along the southernmost coast (Short, 2005). The inner part of the Exmouth Gulf is characterized by water depths of <20 m (e.g., Orpin et al., 1999) and experiences mean significant wave heights of <1 m (Figure 1a) during austral winter, which are even lower during summer. However, wave heights may exceed 5 m during TCs at the entrance to the Gulf (Eliot et al., 2012).

The study area has a tropical, arid climate with hot and humid summers and warm dry winters (Semeniuk, 1996), moderate southerly winds during summer, and predominantly northerly winds during winter (BoM, 2016a). Favored by high sea surface temperatures (SST) (Emanuel, 2005), it belongs to one of the most TC affected coastlines of the world (Figure 1; Lough, 1998; Short & Woodroffe, 2009), exhibiting a slightly increased TC frequency during La Niña conditions (Chand et al., 2013; Denniston et al., 2015; Kuleshov et al., 2008; Nicholls, 1984). TCs entail temporarily high fluvial, aeolian and, in combination with related storm surges, littoral morphodynamic activity, causing major coastal changes such as beach and foredune erosion, washover deposition, and/or sediment redistribution (Nott & Hubbert, 2005; Semeniuk, 1996). Storm surges play a significant role in erosion (Nott & Hubbert, 2005) and the formation of coastal landforms in the Gulf such as large washover fans at Point Lefroy (SW Exmouth Gulf) and chenier-type ridge sequences in Giralia Bay (SE Exmouth Gulf), representing geological records for past TC occurrence on Holocene time scales (May et al., 2017, 2018). Ten TCs with notable damages in the Exmouth region are listed since December 1875 (BoM 2016b), with category 5 TC Vance (18–22 March 1999; 910 hPa central pressure) being one of the strongest TCs in Australia's history. TC Vance directly traversed Exmouth Gulf from north to south and resulted in a storm tide of 4.9 m at

Exmouth marina and water levels of up to ~7 m above event tide at Tubridgi Point, north-eastern margin of Exmouth Gulf (BoM, 2016c; Nott & Hubbert, 2005). In 2015, TC Olwyn caused a storm surge of ~1 m above storm tide at Exmouth, which was amplified in the southern Gulf area (May et al., 2018).

2.2. Context, Previous Findings, and Pre-Olwyn Washover Geomorphology

The washover deposits at Point Lefroy have been used to reconstruct TC activity over Holocene time scales, characterizing them as a unique geomorphic record (Brill et al., 2017, 2018; Callow et al., 2018; May et al., 2017). This study focuses on the westernmost washover fan at Point Lefroy. It is connected to a ~100 m wide former and presently sealed breach in the present beach-foredune barrier (Figures 1 and 2). This barrier reaches elevations of ~6 m Australian Height Datum (AHD) to the east and west, and its elevation inside the breach remained below 3 m AHD before TC Olwyn, with a width of ~40 m. Steep slopes (>20°–25°) characterized the landward part of this barrier section, dropping down to ~1.5 m AHD. In its north-eastern corner, an area of lower elevations extended into an eastwards-bent linear depression, separating the beach from the main barrier (Figure 2a).

To the south, the washover throat has the form of a NNW-SSE running, broad and linear channel, separating two elevated terrace-like fan sections (termed lateral banks) to the west and east. The surface of the central channel rose to ~2.6 m AHD toward the south, and the lateral banks reached elevations of >3.2 m AHD (Figure 2). The central channel intersects with two W-E-oriented lateral channels commencing directly landwards of the barrier-mudflat boundary. While the channels dropped to an elevation of ~1.5 m AHD at and seaward of this intersection, the spillover elevation of the western lateral channel toward the mudflat was at ~2.3 m AHD.

The higher parts of the lateral banks showed a rather planar surface with a system of smaller channels in its southern part, in particular, at elevations below 2.7 m AHD and/or where the central channel opens into the mudflat. Few NE-SW-directed channels crossed the central and southern parts of the western bank as well as the southern part of the eastern bank, where they were below 2.7 m AHD.

While the eastern bank exhibits a slightly convex cross profile and gradually drops down toward the mudflat (<5°, mostly <3°), steep slopes (>10°, often >20°) characterized the western margin of the fan. Small delta-like lobes were documented where narrow channels dissecting the western bank opened into the mudflat. A similar morphology was present in the southern part of the central channel, although absolute elevation differences were smaller. Here, a ~150 m wide and ~10–20 cm high sand lobe stretched southwards into the mudflat.

2.3. Pre-Olwyn Washover Chronostratigraphy

The washover fans at Point Lefroy consist of an up to 2 m thick sequence of sand, shell debris, and coral rubble deposits alternating with intermediary palaeosols. In previous work, May et al. (2017) presented a detailed characterization of the washover fans' stratigraphical architecture and chronostratigraphy based on optically stimulated luminescence (OSL; cf. Brill et al., 2017, 2018). In addition, Callow et al. (2018) presented a novel KMeans classification approach based on using the R-G-B-data of objects within a remotely piloted aircraft system (RPAS) SfM point cloud to identify bare-earth points and, ultimately, to create a high-resolution Digital Terrain Model (DTM) of the washover fan. The combination of high-resolution chronostratigraphical and geomorphological data allowed for establishing a local long-term TC record, suggesting periods of increased storm-induced deposition at ~170, ~360, ~850, and ~1,300 years ago, with further units dated to ~1,950, ~2,300, and ~2,850 years ago. As correlation with ENSO proxies suggests a causal link of TC occurrence and ENSO in the northern part of WA, the findings underline the regional palaeotempestological relevance of this unique geomorphological record.

2.4. Recent to Subrecent Washover Activity

TC Vance in March 1999 induced morphodynamic activity in particular at the western bank of the washover fan (May et al., 2017; Figure 1b). Later, between 2002 and 2013, no activity is documented based on Google Earth satellite images (Figures 1c and 1d). Similarly, post-TC Olwyn satellite images from October 2015 docu-
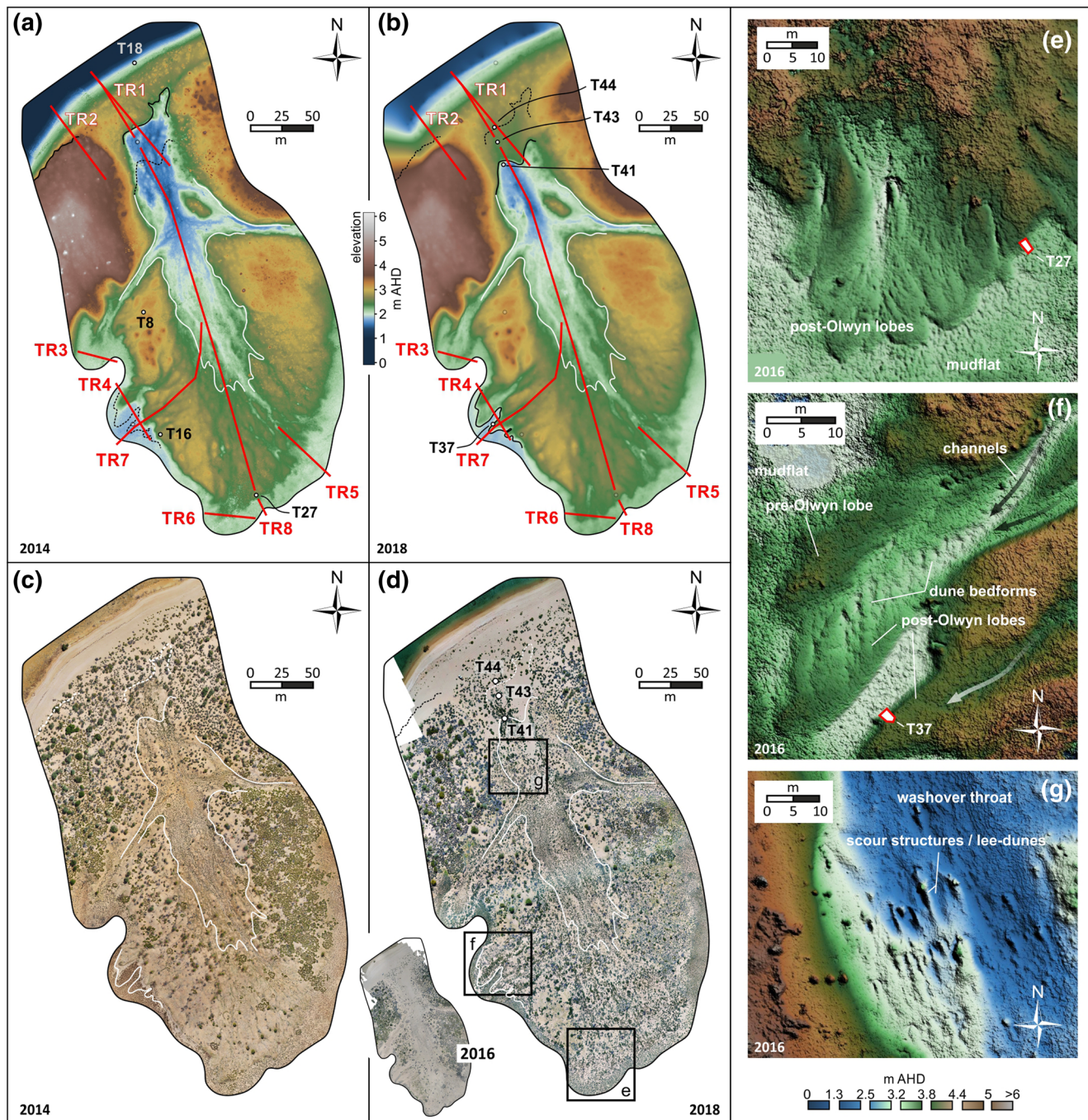
Figure 2. High-resolution DTMs (5 cm) and orthophoto mosaics (1 cm) of the investigated washover fan of 2014 (a and c), 2018 (b and d), and 2016 (kite data; inlay in d, e–g). Locations of trenches (T) and cross sections (TR) are depicted. The geomorphological interpretation of the fan is based on the DTMs. While the present SW–NE-running barrier reaches 4.5–6 m AHD, the lateral banks of F1 show a maximum elevation of 3.3 m AHD. Two lateral channels run to the southeast and south-west. A broad runup channel forms the washover throat that passes into a distributary network toward the distal fan. (e) Kite-based DTM of post-TC Olwyn sediment lobes in the landward part of the central washover channel, at the transition to the mudflat. (f) Post-TC Olwyn lobes (kite-based DTM) at the western lateral margin of the western bank, and channels crossing the western lateral bank; note dune structures at the surface of the sediment lobe. (g) Scour structures and post-overwash lee dunes (kite-based DTM) related to bushes in the seaward part of the washover throat. DTM, Digital Terrain Model.
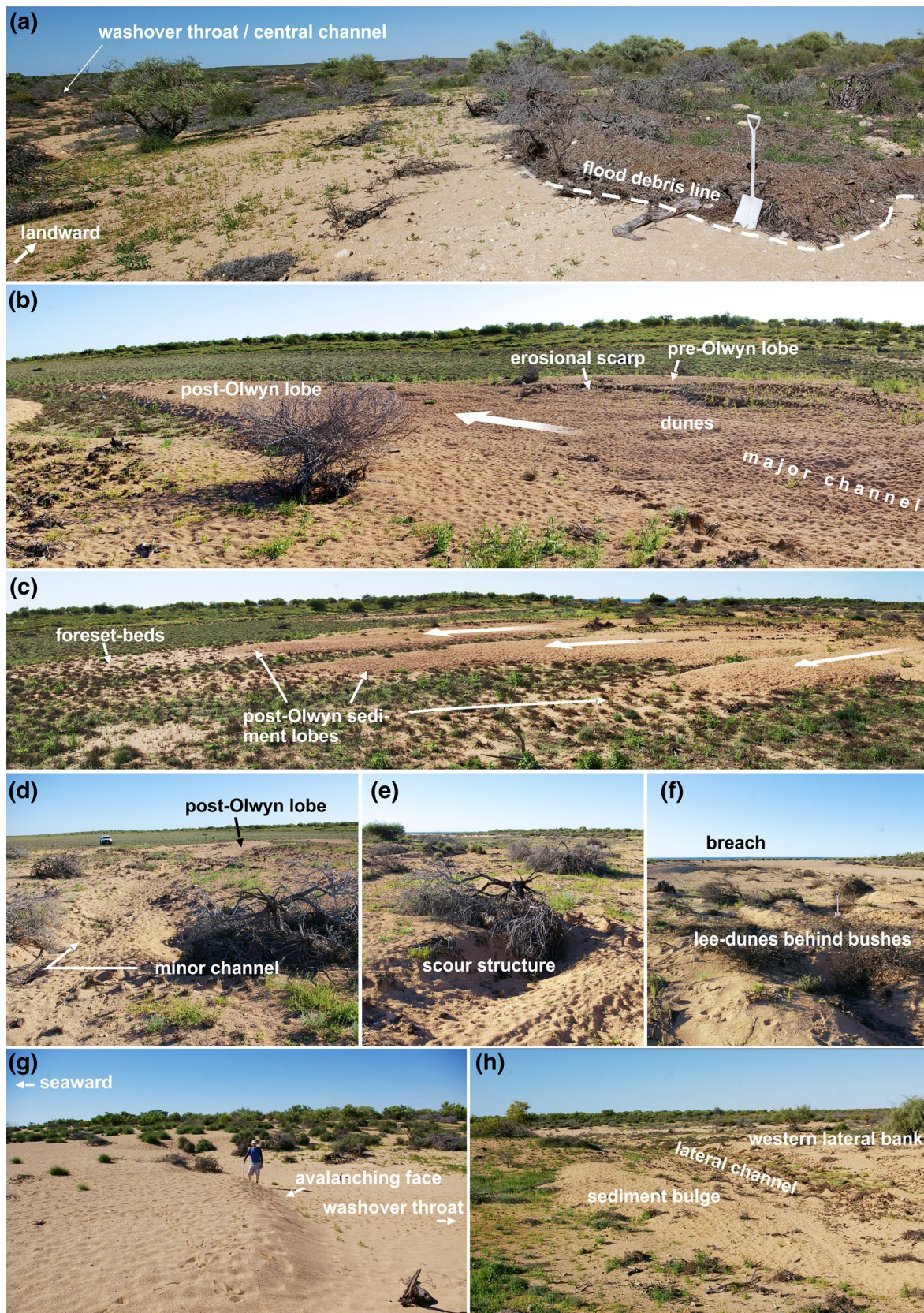
ment depositional activity in the form of new sand lobes and erosion in the washover throat, along the western bank of the washover fan, and in the southern part of the central channel (Figure 1; May et al., 2017).

3. Methods

3.1. Field Survey, Trenching, and Sampling

Post-Olwyn field surveys were carried out in 2016 and 2018. Field work included geomorphological surveys and the documentation of post-Olwyn flood marks (Figure 3a). Trenches were dug on top of new/fresh sediment lobes deposited by TC Olwyn and in back-barrier sections of the washover throat which has been filled with sediments by TC Olwyn (T37, 41–44; Figures 2–6). In addition, trench T27 was dug in the landward part of the central channel, at the transition to the adjacent mudflat, in August 2014. This area was assumed to represent deposits of TC Vance according to the interpretation of satellite images (Figure 1). All trenches were described and photographically documented (Figures 7 and 8), before samples for luminescence dating were taken from trenches T27, T37, and T43.

3.2. Remote Sensing (UAV and SfM) in 2014 and 2018

Pre-Olwyn imagery was captured in 2014 and has been published within Callow et al. (2018). The data can be accessed via the data repository of the University of Western Australia (Callow, 2020). Imagery was collected using an 18-megapixel (Mp) Canon EoS-M DSLR camera (22 mm prime lens) on a rotary-wing RPAS at 50 m altitude (0.9 cm ground pixel), capturing every 2 s to achieve 91% frontlap and 50% sidelap. The data set comprised 1,208 images collected across 10 flights between 8 a.m. and 2 p.m. on a cloud-free day in August 2014, flown as east-west transects from south to north across the fan to minimize any differences in light intensity, sun-angle, and shadow between images. Ground control was from 32 points (17 control, 15 validation) surveyed using a Real-Time Kinematic Differential Global Positioning System (RTK-DGPS; Topcon Hiper Pro, manufacturer's accuracy horizontal: 10 mm + 1.0 ppm and vertical: 15 mm + 1.0 ppm).

Post-Olwyn imagery in 2018 (1,264 images) was captured by DJI Phantom4 Advanced (20 Mp, 24 mm lens; 35 mm equivalent—Model FC6310) at 50 m altitude (1.4 cm ground pixel), capturing every 2 s at 90% frontlap and 75% sidelap, across two flights around solar noon (12:00–1:00 p.m. local time), with similar north-south camera orientation flying east-west transects. The data can be accessed via the data repository of the University of Western Australia (Callow, 2020). Ground control was from 40 points (34 control, 6 validation; Trimble R10 RTK-DGPS, mean per-point survey accuracy horizontal: 15 mm, vertical: 29 mm). The 2018 site was tied into AHD (to relate to tidal and storm surge data), using a 7 h GNSS log, postprocessed using AUSPOS to 15 processed baselines, yielding an absolute AHD position of 57 mm X, 60 mm Y, and 50 mm Z of absolute position relative to AHD.

While imagery from 2014 has previously been processed and published by Callow et al. (2018), it is known that different software versions can produce different results from cloud optimization, and best-practice is to set physically realistic and not software manufacturers default optimization parameters (i.e., reference settings, see James et al. 2017). Both years were (re)processed in Agisoft Metashape (v1.5), photo alignment on high, with poor-quality points from the sparse cloud iteratively removed (per-point error: Reprojection error > 0.5, Reconstruction Uncertainty > 20). Bundle adjustment and sparse cloud optimization used real-world individual marker error where available (RTK-DGPS manufacturers error for 2014 data sets and per-point survey error 2018, Measurement Marker Accuracy 0.02 m 2014; 0.015 2018), and Image Marker Accuracy was set to the actual value from marker alignment in each data set and similarly for Tie Point Accuracy (set to the Point Cloud RMS reprojection). Camera Model C (f, c1, c2, k1, k2, k3, p1, and p2) recommended by James et al (2017) and

Figure 3. Post-Olwyn photos of the washover fan taken in August 2016. (a) Flood debris line at ~4.20 AHD, just west of the washover throat (cf. Figure 5b). (b) Sediment lobe of TC Olwyn with dune structures related to one of the main channels crossing the western lateral bank. (c) Three major sediment lobes deposited by TC Olwyn along the western margin of the washover fan. The thin sediment cover ahead the sediment lobes are interpreted as foreset-bed type sediments. (d) Minor channels and scouring on top of the western lateral bank. (e) Scour structures in the southern part of the central channel. (f) Scour structures and postevent lee-dunes in the seaward part of the central channel. (g) Avalanching face at the new landward margin of the barrier, at the transition to the washover throat. (h) Semicircular sediment bulge at the landward end of the western lateral channel. AHD, Australian Height Datum; TC, tropical cyclone.
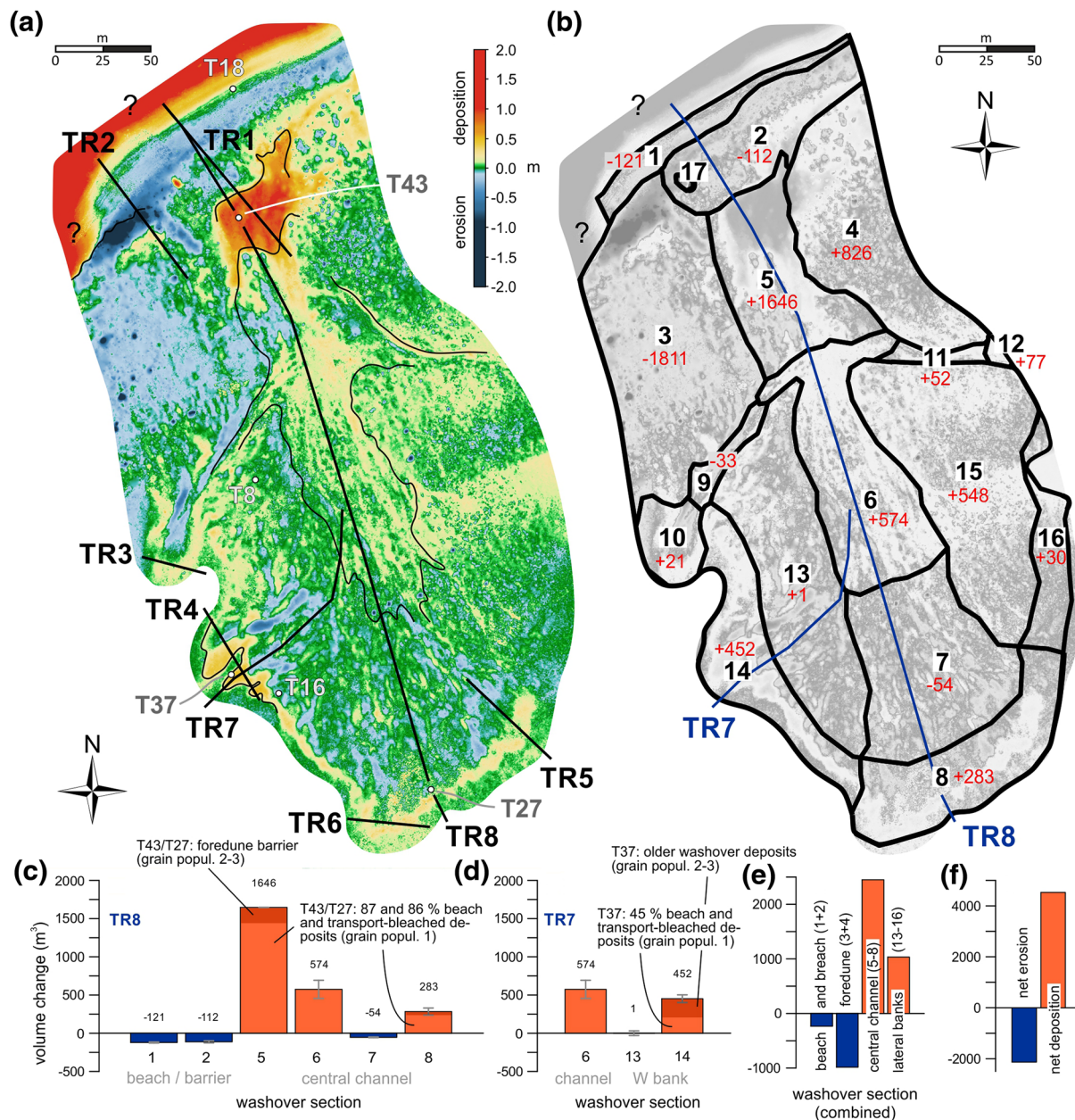
Figure 4. (a) Pattern of erosion and deposition based on the comparison of the 2014 and 2018 DTMs. Deposition was also inferred in the intertidal area, but caution is needed due to different tidal conditions and water levels during UAV surveys in 2014 and 2018. However, deposition mainly occurred in the center and along the southern margin of the central channel, along the western lateral margin of the fan, and directly behind the pre-Olwyn barrier inside the breach. Significant erosion was also mainly found in the lower parts of the western lateral bank, in the southern part of the central channel, and along the beach and (particularly western) foredune. (b) Greyscale version of image shown in (a) with washover fan subenvironments (i.e., washover sections; cf. Table S4) and sediment volume changes (in m³; positive/negative numbers refer to net deposition/erosion within each section). (c) Erosion and deposition calculated for washover sections 1, 2, and 5–8 along TR 8. Sediment provenance (light and dark orange colors) for washover sections 5 and 8 are based on luminescence data found for samples T43-1 and T27-1, that is, the percentages of grain populations P1-3. (d) Erosion and deposition calculated for washover sections 6, 13, and 14 along TR 7. Sediment provenance (light and dark orange colors) for washover section 14 is based on luminescence data found for sample T37-1, that is, the percentages of grain populations 1-3. (e) Cumulated erosion/deposition volumes combining sections 1 and 2 (beach and young barrier inside breach), 3 and 4 (W and E foredune barriers), 5–8 (washover throat/central channel), and 13–16 (lateral banks). Net sediment erosion in the seaward sections of the washover (mainly the beach and barrier) is opposed to net sediment deposition in the washover throat and along the lateral banks, likely reflecting typical barrier rollover processes. (f) Total volumes of erosion and deposition integrated over all washover sections. Deposition exceeds erosion by a factor of 2, suggesting that additional sediment was transported to the washover fan from sediment sources not captured in the DTMs, that is, the sub- to intertidal zone and/or the adjacent barrier sections. For further explanation of washover section numbers, the reader is referred to the main text and Table S4 in the supplementary materials. DTM, Digital Terrain Model; UAV, unmanned aerial vehicle.
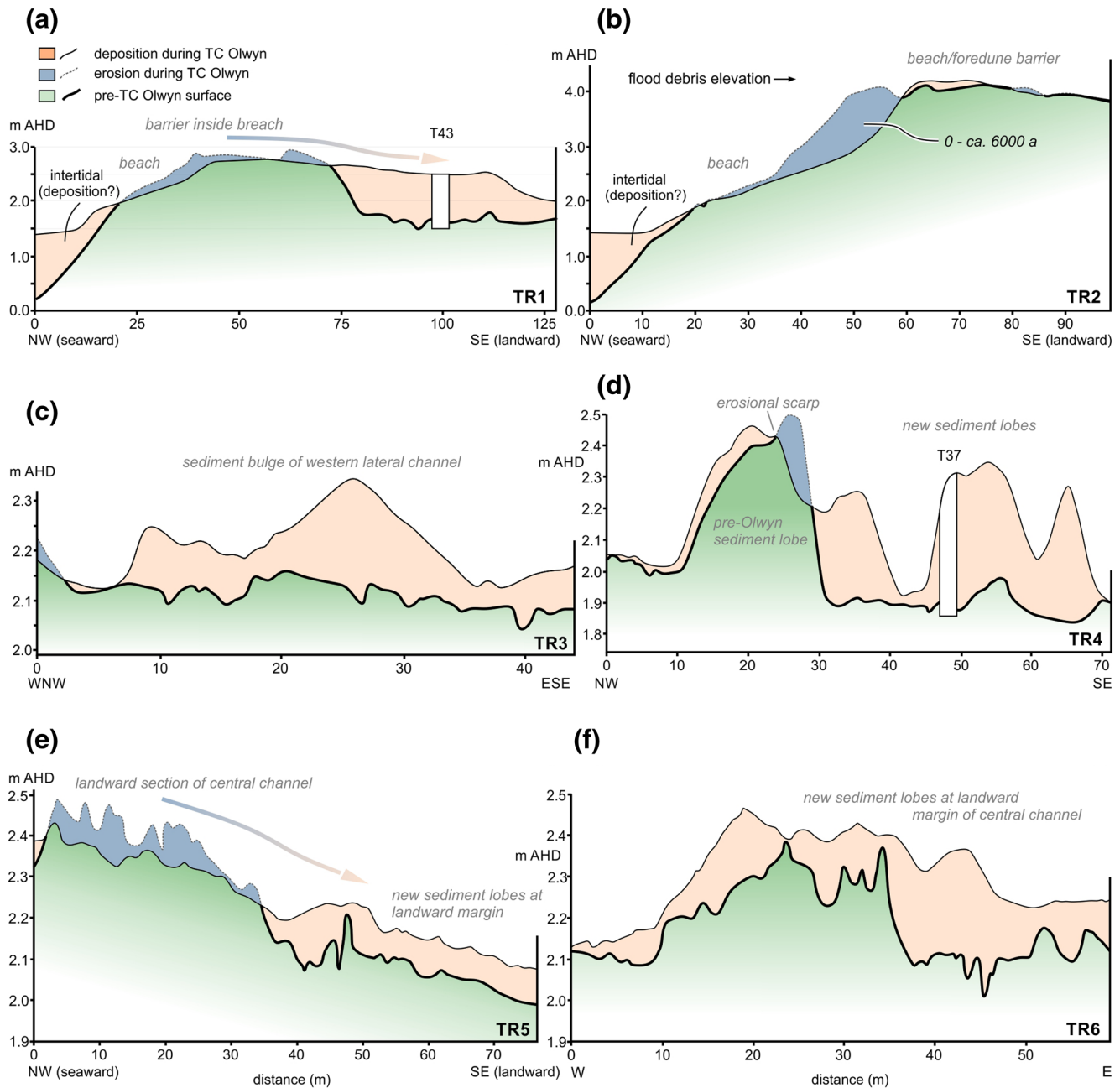
Figure 5. Cut-and-fill profiles along topographical transects TR 1–6 (see Figures 1, 2 and 4). (a) While the uppermost 10–20 cm of the pre-Olwyn barrier inside the breach were eroded, the barrier width increased by ~50 m. (b) To the west of the breach, erosion occurred along the foredune barrier. (c) A semicircular sediment bulge of ~20 cm height was deposited at the transition from the lateral channel to the back-barrier mudflat. (d) New sediment lobes formed along the western lateral margin of the washover fan; a prominent pre-Olwyn sediment lobe was partly eroded (erosional scarp, cf. Figure 3b). (e and f) New sediment lobes of ~10 cm thickness formed along the landward margin of the central channel, likely sourced by erosion of directly adjacent pre-Olwyn deposits in the channel.

proven to be optimal for the 2014-data set by Callow et al. (2018) was applied. The check point or validation error using markers (ground control points, GCPs) not used in any optimization was an absolute total (*XYZ*) accuracy of 51 mm (39 mm *X*, 29 mm *Y*, and 14 mm *Z*) for 2014 and 30 mm (8 mm *X*, 12 mm *Y*, and 27 mm *Z*) for 2018. Sparse clouds (5,003,315 points 2014; 3,038,230 points 2018) were filtered using the KMeans approach of Callow et al. (2018), based on 20 clusters built from sampling 2% of the R-G-B 3-band *XYZ* sparse cloud, and
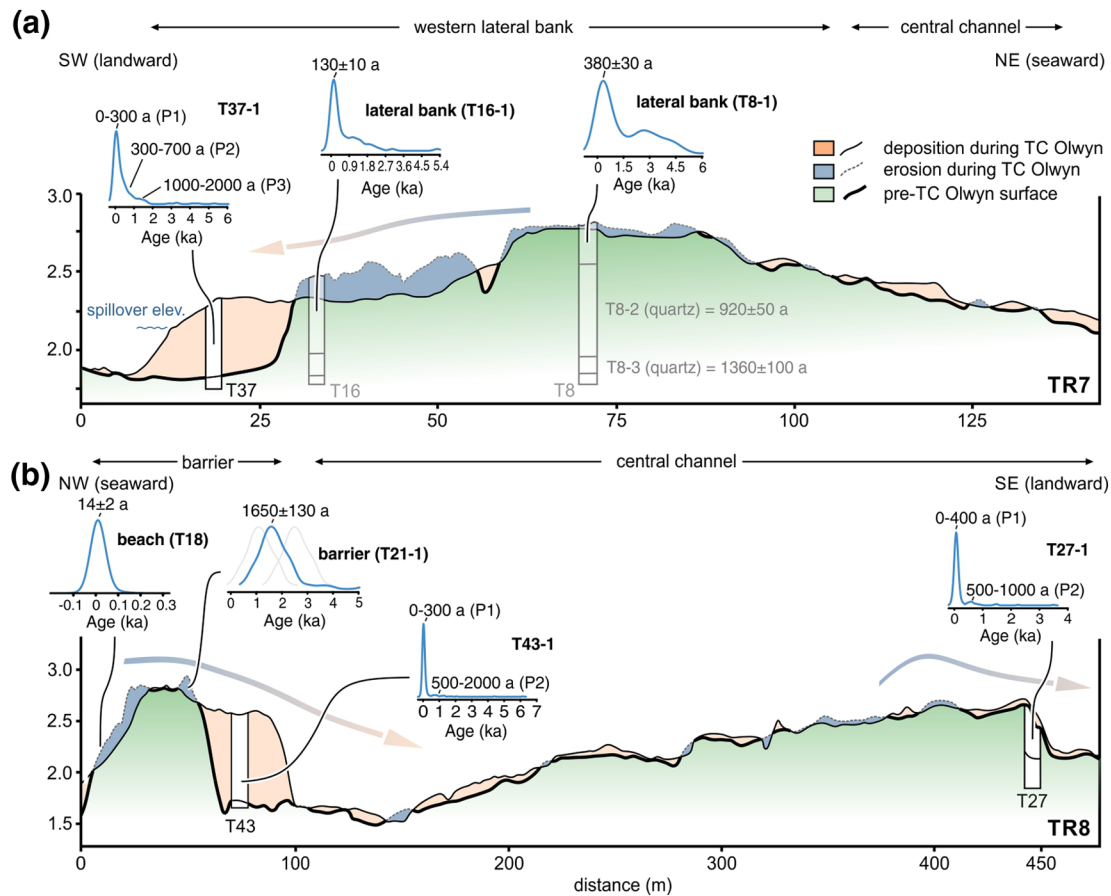
Figure 6. Cut-and-fill profiles along topographical transects TR 7 and 8 (see Figures 1, 2, and 4) including different populations in the quartz-based age distributions, which were documented for samples from trenches along the transects. Data from T8, T16, T18, and T21 taken from May et al. (2017) and Brill et al. (2017, 2018). In the center of the western lateral bank (T8), only the uppermost (youngest) depositional unit was affected by erosion; the underlying units were dated to ~920 and 1,360 a (e.g., May et al., 2017).

then selecting bare-earth clusters. Bare-earth points (1,050,513 points 2014; 1,114,743 points 2018) were then built into a DTM.

When 2014–2018 data was compared, an error in the recorded height of the RTK Antenna was noted from the 2014 imagery and confirmed using field photos (incorrect vertical height set). The corresponding vertical offset of +1.010 m was corrected for the 2014 DTM, and the two data sets where coregistered vertically, by sampling the height of five 2014 GCPs. All GCPs were located on the mudflat that was not subject to any observable sedimentation or erosion as compared to the 2018 surface and were selected based on careful field and ortho-photo-mosaic inspection. The resulting mean error of the corrected surface was 0.020 m for the vertically coregistered 2014 GCP points. Planimetric (XY) coregistration was necessary as each data set was based on independent processing of the two base locations using AUSPOS, which introduces potential significant compounding error of the relative (within survey) and then absolute (to AHD) error. We coregistered 2014 to the 2018 data set (against 2018 Datum "UWA-EX01") using fixed points within the site including unmoved stones, large fallen (unmoved) branches away from the inundated area, and exposed corals and rocks, improving the initial mean XY error of 0.56 m, (shifting +0.541 m X and +0.147 m Y). We created a high-resolution map of erosion and deposition during TC Olwyn (Figure 4), by subtraction of the 2014 DTM from the 2018 DTM using ArcGIS. These data can be accessed via the data repository of the University of Western Australia (Callow, 2020). Using the approach of Wheaton et al. (2010), cumulative mean error of the two DEM data sets is the detectable change, with cumulative vertical error 38 mm (X = 78 mm, y = 81 mm, Mean XYZ error 119 mm). Finally, post-Olwyn sediment volume changes were calculated for different washover sections (Figure 4, Table S4) for all pixels
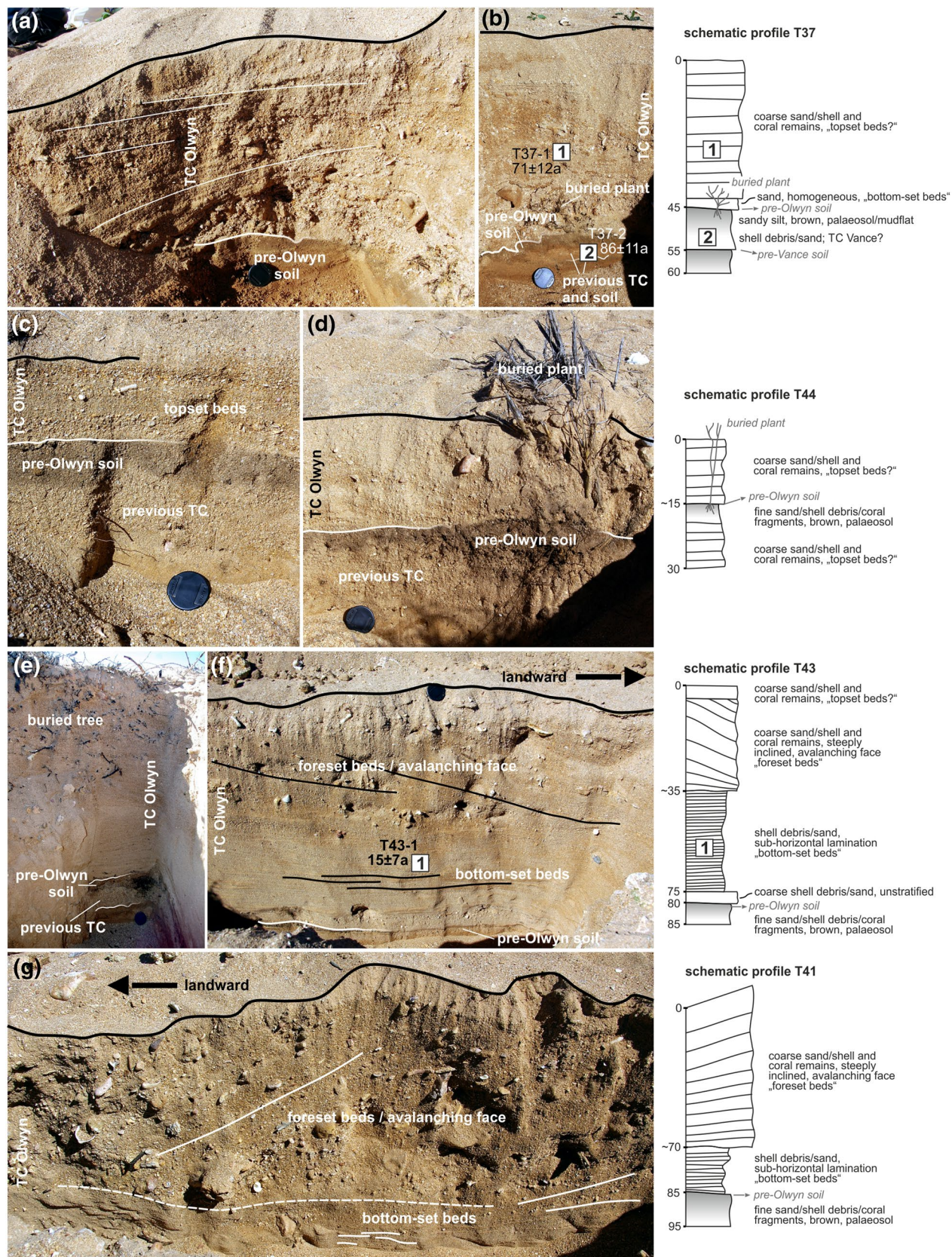
Figure 8. Stratigraphy and chronology of trench T27 (cf. May et al., 2017). Two depositional units were documented, separated by an organic-rich layer (paleo-surface). The upper unit is assumed to be related to TC Vance in 1999, which impacted the washover fan in this area according to satellite images (cf. Figure 1). TC, tropical cyclone.

above (+0.078 m) or below (−0.078 m) the detectable limit thresholds. All data between these thresholds were set to zero. Volumes are given as the sum of volume change in cubic meters and include uncertainties.

3.3. Remote Sensing (Kite Survey and SfM) in 2016

In between the previously described acquisitions, a kite-based low-cost survey was conducted on August 12, 2016. The kite was equipped with a GoPro HERO3+ black edition with a 12 MP resolution, using a 20 mm lens (35 mm equivalent) and capturing images every 1 s between 9:00 and 15:00 local time. The resulting 10,416 pictures were surveyed and images of poor quality or unsuitable aspect were removed, reducing the data set to 1,248 images. This reduction still resulted in a full coverage of the target area and a high overlap of nine or more images for each pixel, thereby significantly reducing computation time. The final image data set was used in the same software package mentioned above, with camera type set to "fisheye." Ten control points equally covering the entire area were manually selected, representing unmoved larger stones or the center of stable shrubs. All control points were also identified in the georeferenced Digital Orthophoto (DOP) of 2014; coordinate information was used from this DOP; elevation was taken from the corresponding DTM. Here, the accuracy of the GCPs was set to 2 cm and resulted in an overall accuracy (XYZ) of 35 cm (12 cm X, 24.7 cm Y, and 22.2 cm Z). The final point cloud contained 99 Mio. points, resulting in a DTM with a 4.32 cm resolution and a DOP with a resolution of 2.16 cm. Generally, the final products visually fit to the previous (2014) and subsequent (2018) data sets, though some minor inaccuracies remained. Thus, this DTM was only used for detailed illustration of particular washover sections, whereas the pre- and post-Olwyn DTM comparison and the pattern of erosion and deposition is based in the 2014 and 2018 imagery (Figures 2 and 4).

3.4. Luminescence Measurements

Sediments deposited by TC Olwyn in March 2015 were sampled in July 2016, that is, ~16 months after the event. We sampled a prominent sediment lobe, which had developed during TC Olwyn along the western fan margin (T37-1). T37-2 stems from the pre-Olwyn sand unit just below the soil surface underlying the TC Olwyn deposit. Sample T43-1 was taken from the fresh barrier deposit inside the breach, which accreted landward of the pre-Olwyn barrier by ~30 m during TC Olwyn. In addition, T27-1 and T27-2 were sampled in August 2014, ~8 months before TC Olwyn. T27 is located at the landward end of the washover throat, at the transition to the mudflat. Deposits of T27 are assumed to have been deposited by TC Vance in 1999 (T27-1) and by a pre-Vance TC (T27-2), which had been identified during previous work (Brill et al., 2017; May et al., 2017).

Figure 7. (a) Stratigraphy and chronology of trenches T37 (a and b), T44 (c and d), T43 (e and f), and T41 (g). Deposits of TC Olwyn are well-stratified and overly the pre-Olwyn soil/surface. In T37 and T43, a predecessor TC event can be inferred from a basal sand layer at the bottom of the trenches; this unit was OSL dated to 86 ± 11 a and is assumed to be related to TC Vance in 1999. In T41-44, bottom-set beds, foreset beds, and topset beds are distinguished. No. 1 and 2 in (b and f) refer to the OSL sample numbers. TC, tropical cyclone.

Luminescence measurements were carried out at the Cologne Luminescence Laboratory and included age determination, quartz and feldspar signal comparisons, as well as the assessment of bleaching proxies including remnant ages and percentages of fully bleached grains (i.e., grains that agree with the control age within their 2-sigma uncertainties). Optically stimulated luminescence (OSL) measurements of quartz and infrared stimulated luminescence (IRSL) measurements of potassium feldspar single grains were performed for all samples collected in 2016 (T37 and T43). For T27, only OSL measurements of quartz single grains were carried out.

The determination of luminescence burial ages requires the estimation of the energy dose accumulated since the last event of light exposure (i.e., the burial dose) and the amount of ionizing radiation affecting the sample per unit of time (i.e., the dose rate). Dose rate determination (summarized in Table S1) was based on the DRAC software version 1.2 (Durcan et al., 2015) and using U, Th, and K contents from high resolution gamma spectrometry and in-situ water contents. Internal feldspar dose rates were based on potassium contents of $10 \pm 2\%$ (Smedley et al., 2012). Samples for burial dose determination (summarized in Table S2) were dry-sieved (150–200 μm), treated with 10% HCl and 10% H_2O_2, density-separated (potassium feldspar < 2.58 g/cm^3 < 2.62 g/cm^3 < quartz < 2.68 g/cm^3), and etched with 40% HF in the case of quartz. For each sample, 500–600 single grains of quartz and potassium feldspar were measured on a Risø TL/OSL reader, with a combination of green laser and a U340 filter for quartz, and IR laser and a 410 nm interference filter for feldspar. Measurements of quartz followed the single aliquot regenerative dose protocol (Murray & Wintle, 2003) with specifications described and evaluated for sediments from the same location by Brill et al. (2017) (Table S3a). For measurements of potassium feldspar, a post-IRSL$_{150}$ protocol (Table S3b) was used, evaluated for sediments from the same site by Brill et al. (2018). The post-IRSL$_{150}$ protocol provides doses based on the IRSL signal measured at 50°C (IRSL) and the post-IRSL signal measured at 150°C (post-IRSL$_{150}$) on the same grains. The applicability of the protocols to samples used in this study was tested by means of successful dose recovery tests with dose-recovery ratios of 0.99–1.01 for quartz and 0.97–1.02 for feldspar IRSL and post-IRSL (Figure S1).

Single grain dose distributions were transformed into age distributions by dividing individual equivalent dose values with sample-specific environmental dose rates. The potassium feldspar IRSL age distributions were further corrected for athermal signal loss over the burial time (i.e., anomalous fading). Experimental g-values between 3.5 ± 0.1 and $3.9 \pm 0.1\%$/decade (Figure S1, Table S2) were determined using the approach of Auclair et al. (2003) and used for fading correction according to Huntley and Lamothe (2001). No fading correction was performed for the post-IRSL$_{150}$ ages due to g-values <1.5%/decade. Finally, remnant ages of 30 a (IRSL) and 50 a (post-IRSL$_{150}$) that were shown to remain in modern beach samples from the washover site (Brill et al., 2018; supported by laboratory residual measurements on the post-TC Olwyn samples, Figure S1), were subtracted from the fading-corrected IRSL and the post-IRSL$_{150}$ age distributions.

Calculation of burial ages from the dose distributions was done by means of the bootstrapped version of the minimum age model (MAM$_{bs}$, Cunningham & Wallinga, 2012). Following the approach described by Chamberlain et al. (2018), σ_b values of $28 \pm 3\%$, $41 \pm 2\%$, and $40 \pm 3\%$ for quartz, IRSL, and post-IRSL$_{150}$, respectively, were calculated (Figure S2) by applying the MAM$_{bs}$ to the over-dispersion values of all samples ($n = 23$ for quartz and $n = 18$ for feldspar; based on data from this study, Brill et al., 2017 and Brill et al., 2018). Since the unlogged version of the MAM$_{bs}$ had to be used for the very young samples of this study (Arnold & Roberts, 2009), relative σ_b values (in percentage) were transformed to absolute values (in Gy, Table S2) by multiplying percentages with MAM-derived ages in an iterative procedure. To identify statistically distinctive grain populations in the age distributions of the quartz samples, the finite mixture model (FMM, Galbraith & Roberts, 2012) was applied.

4. Results

4.1. Geomorphological Impact of TC Olwyn

As no significant storm surge occurred between the 2014 and 2018 UAV surveys (Figure S5), the observed geomorphological changes can clearly be attributed to TC Olwyn. Flood marks in the form of thick piles of wooden debris were documented particularly along the lateral margins of the washover throat at ~4 m AHD (Figure 3a). Based on the comparison of pre- and post-TC Olwyn DEMs, intense erosion was observed along the recent beach and barrier just west of the washover throat entrance (Figures 4a and 4b). Here, ~25 m of the beach and foredune barrier deposits were eroded up to a thickness of 2 m along a ~35 m long barrier section (TR2, Figures 4–6). In addition, minor erosion of <20 cm occurred on top of the western foredune barrier, be-

tween the beach and the western lateral channel, as well as on the surface of the pre-Olwyn barrier inside the breach. Erosion in these washover sections amount to altogether ~2050 m³ of sediment (washover sections 1–3, Figures 4b–4e).

In contrast, sedimentation was highest in the seaward sections of the eastern foredune barrier (~826 m³ net sediment accumulation in washover section 4, Figure 4b) and particularly of the washover throat (washover section 5, 1,646 m³, Figures 4b and 4c), directly landward of the pre-Olwyn barrier (TR 1 and 8, Figures 5 and 6). Southward progradation of the barrier amounts to 30–40 m, that is, the post-Olwyn barrier stretches 40 m further into the washover throat. The transition to the throat is characterized by a steeply inclined slope, similar to the one found in 2014. Directly behind this drop to the washover throat, scour structures on the throat surface were documented particularly behind obstacles (mostly bushes; Figure 3). Since the scour structures always occur on the landward side of bushes, they are clearly linked to inflowing water.

Fresh sandy deposits were documented along the sides and at the landward end of the two lateral channels (washover sections 10 and 12; ~100 m³, Figure 4b). A distinct semicircular sand deposit was found just south of the western lateral channel, where it opens into the mud flat (TR 3, Figures 3h, 4, and 5c). Particularly along the western lateral channel, lateral erosion of a few decimeters is inferred (washover section 9, −33 m³, Figure 4b), and erosion is documented at the transition to the mudflat inside the semicircular deposit.

Most significant morphological changes concentrated along the western lateral bank of the washover fan, where both erosion and deposition are documented. Distinct channels, some preexisting in 2014, were enlarged and deepened, and new ones formed. On the other hand, a thin sand sheet was deposited in large parts of the lateral bank between the channels, resulting in a net sediment volume change of 1 m³ on top of the western lateral bank (washover section 13, Figure 4b). In the largest channels, found in the center of the western bank, dune structures of ~1–2 m wavelength were observed in 2016, that is, 1 year after TC Olwyn (Figures 2e–g and 3). At the landward end of these channels, new sediment lobes of 15–30 m length formed on top of the pre-Olwyn mudflat (Figures 2–7), amounting to ~450 m³ of sediment (washover section 14, Figure 4b). A prominent pre-Olwyn lobe experienced lateral erosion and accretion (TR4; Figures 3b, 4, and 5). The sediment lobes are indicated by an avalanching face with a steep slope at the transition to the mudflat (TR7), and bottom-set bed type deposits in front of the avalanching faces are visible. In contrast to this western fan section, the eastern lateral bank experienced only minor morphological changes. However, a thin layer of fresh sediment (generally <10 cm) was observed particularly in the seaward section of the lateral bank, and few centimeter of erosion may be inferred on the surface as well (Figure 4), altogether resulting in the accumulation of ~550 m³ of sediment.

Major deposition also took place in the landward section of the central channel (+574 m³, washover section 6, Figure 4b), which is characterized by numerous bifurcation channels. A thin (<30 cm) and ~5 m wide sediment sheet accumulated where the central channel opens into the mudflat, that is, at the transition from the central channel to the mudflat (+283 m³, washover section 8, Figure 4b). A distinct sediment lobe built in the SW of the main channel (TR5 and 6). Scouring occurred particularly behind vegetation (Figure 3e), but erosion and deposition were observed at many places, generally reflecting the linear pattern of the bifurcation system (Figure 4).

4.2. Sedimentology, Stratigraphy, and Luminescence Inventories of Modern Analog Deposits

4.2.1. Stratigraphy of Trench T37 (Western Lateral Bank, TC Olwyn)

Trench T37 consists of a 45-cm-thick and well-stratified sequence of sand, shell debris, and coral remains overlying the pre-Olwyn soil (Figures 7a and 7b). Individual layers of the sand unit are inclined toward the mud flat, and finer (gravelly sand) and coarser (sandy gravel) layers of 1–5 cm thickness alternate. Coarsest sediments were found at the base of this upper unit, containing coral debris of >5 cm. In its basal part, plant remains are embedded into the deposit, belonging to a 15 cm high shrub on the pre-Olwyn mudflat.

Below the reddish dark brown silty to clayey sand of the pre-Olwyn soil, a further ~4 cm thick sand layer was documented. This sand layer covers a second soil surface of red-brown silty to clayey sand, which is assumed to represent the mudflat surface prior to TC Olwyn's predecessor.
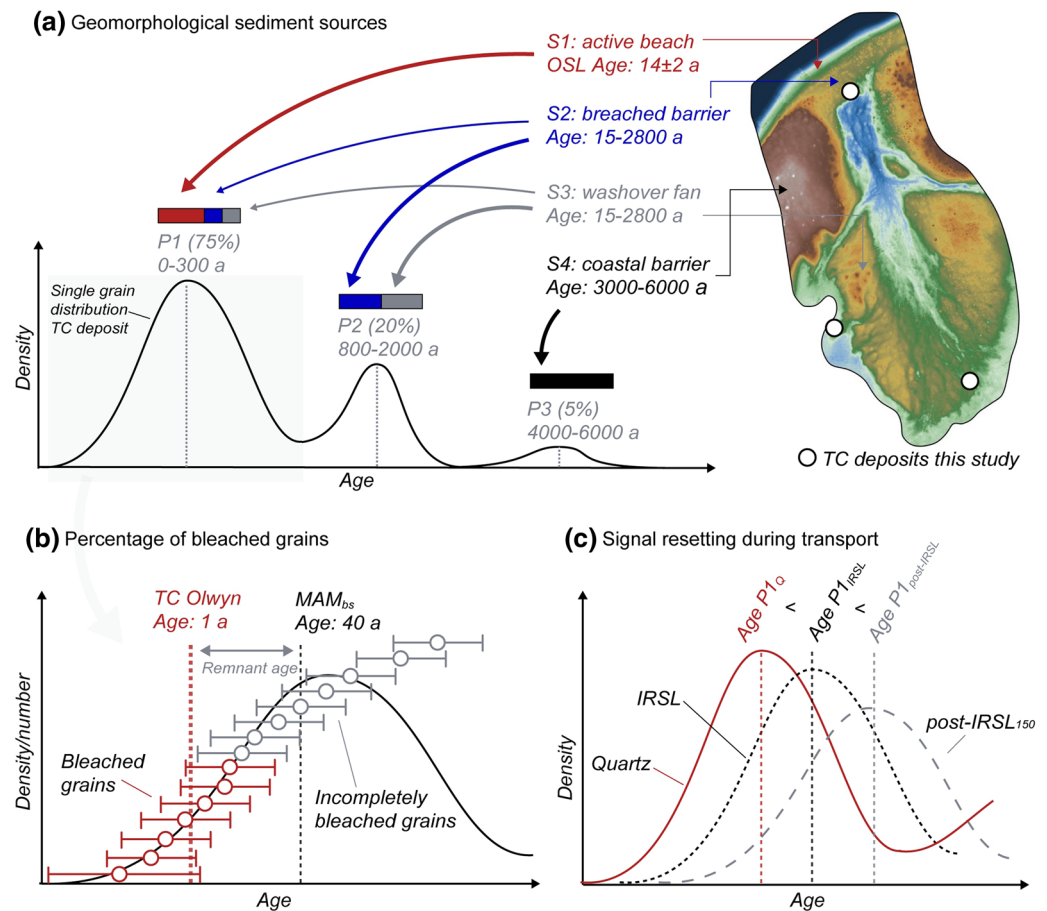
Figure 9. Luminescence inventories as indicators for sediment dynamics (schematic). (a) Comparison of single grain age distributions of TC deposits with chronological information of potential source environments provides information on transport pathways. Note that this is a schematic idealized multimodal distribution, which is not based on measured or synthesized data. (b) The percentage of well-bleached grains in TC deposits (i.e., grains with ages in agreement with age control within 2-sigma uncertainties) is used as a maximum indicator for sediment derived from the active beach. (c) Luminescence ages for the same grain population but based on signals with different bleaching sensitivity (quartz, IRSL, post-IRSL) are used to infer OSL signal resetting during storm transport. IRSL, infrared stimulated luminescence; OSL, optically stimulated luminescence; TC, tropical cyclone.

4.2.2. Stratigraphy of Trenches T41–44 (Landward Part of Barrier Inside Breach, Washover Throat, TC Olwyn)

Trenches T41, 43, and 44 (Figures 7c–7g) illustrate the progradation of sediments landward of the pre-Olwyn barrier inside the breach. At T44, 15 cm-thick stratified sand was found on top of the pre-Olwyn surface (Figures 7c and 7d). The upper 2–3 cm of this surface were enriched with organic material, representing the pre-Olwyn initial soil. Landward of the pre-Olwyn barrier, TC Olwyn accumulated a thick sequence of probably beach-sourced sediments in T43 and 41 (Figures 7f and 7g), and in T42 between these trenches (not shown). In these trenches we found bottom set bed-type deposits (subhorizontal layering of medium to coarse sand) at the base, covered by steeply inclined and coarse (coarse sand and gravel-sized shells and coral) foreset beds and subhorizontally laminated topset beds.

Foreset beds were best developed at the very southern margin of the deposits (T41; Figure 7g). Here, foreset bed-type sedimentation with inclined layers of coarse bed load material (coral, shells, and rocks), related to the avalanching face at the transition to the washover throat, were found on top of a thin unit of finer bottom set bed layers. In T42 and 43, TC Olwyn-deposited sediments are generally finer (predominantly medium sand),
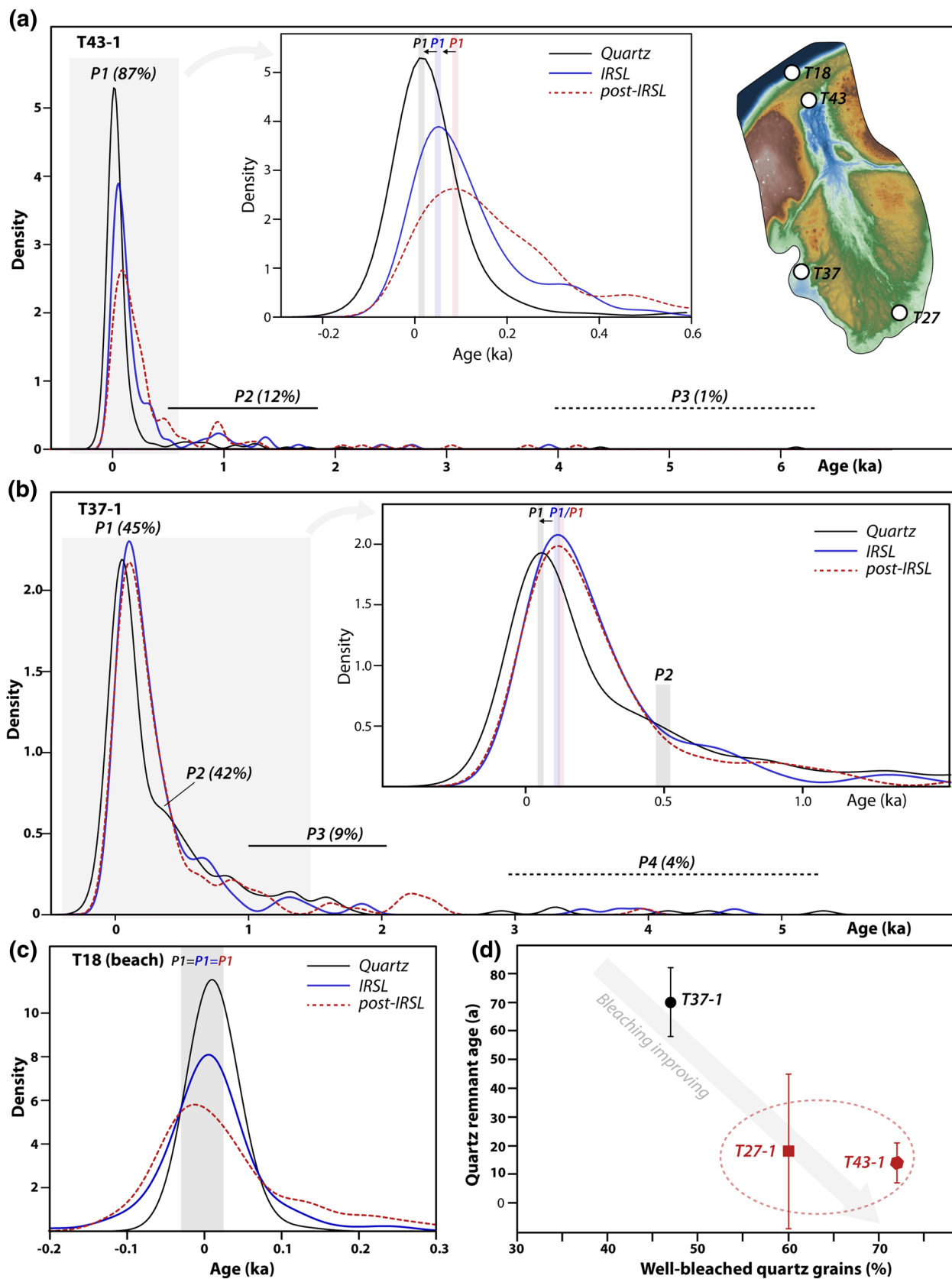
mainly consisting of a horizontally laminated unit (~40 cm) at the base, which is overlain by 30–40 cm coarser and inclined foreset-type deposits (Figures 7e and 7f). In T43, a large bush was buried in the Olwyn-laid sediments (Figure 7e).

4.2.3. Stratigraphy of Trench T27 (Pre-Olwyn Deposits, Landward Margin of Central Channel)

T27 is located in the southernmost part of the fan, at the transition from the central channel to the ~10–20 cm high sand lobe stretching into the mudflat (Figure 8; cf. May et al., 2017). Two sedimentary units were found on top of the silty mudflat deposits in the landward part of T27 (35–22 cm b.s. and 22–0 cm b.s.). Both units coarsen upwards from well-sorted medium sand to gravelly sand. They are separated by a 2 cm-thick brown, organic-rich layer, which tapers out in the seaward part of the trench. Here, the lower unit (59–40 cm b.s.) consists of a basal coarsening-up sequence, followed by a sequence of landwards inclined coarse (gravel-sized coral and mollusc fragments) and fine (sand) layers between 40 and 17 cm b.s. Separated by an erosional boundary, the overlying unit consists of several landward dipping layers of sand, shell debris, and gravel-sized coral and mollusc fragments. The erosional boundary is stratigraphically related to the organic-rich layer separating the two units in the landward part of T27.

4.2.4. Luminescence Inventories of T27, T37, and T43

The OSL, IRSL, and post-IRSL$_{150}$ age distributions of all five samples (Figures S3 and S4) were based on 121–315 grains per sample, which equals percentages of sensitive grains in the range of 35–50% for quartz and 30–40% for potassium feldspar (Table S2). All single grain age distributions showed large scatter with over-dispersion values > 100% for all samples and signals, except from T43-1 (post-IRSL$_{150}$) with only 45 ± 10% (Table S2). The age distributions reached from negative ages to maximum ages of up to 7,000 a for individual grains. All distributions were multimodal with 2–4 grain populations that could be discriminated statistically using the FMM (Figures S3 and S4 and Table S4).

The quartz age distributions of sediments formed by TC Olwyn (T37-1 and T43-1) and probably TC Vance (T27-1) are plotted in Figure 6 and Figure S3. T37-1 revealed four grain populations (Table S4, Figure 10b) with age ranges of 0–300 a (P1, 45% of the grains), 300–700 a (P2, 42%), and 1,000–2,000 a (P3, 8%); in addition, ~4% of the grains were scattered at 3,000–5,000 a (P4). Sample T43-1 yielded grain populations with ages of 0–300 a (P1, 87%) and 500–2,000 a (P2, 12%), and 1% of the grains show scattered ages between 4,000 and 6,000 a (P3) (Table S4, Figure 10a). T27-1 showed age populations at 0–400 a (P1, 86%) and 500–1,000 a (P2, 11%), and another 3% of the grains revealed scattered ages between 1,500 and 3,500 a (P3) (Table S4).

A comparison of the OSL, IRSL, and post-IRSL age distributions of samples T37-1 and T43-1 (Figures 10a and 10b) showed that the well-defined peak of the youngest grain population (P1) shifts from older toward younger ages. The number of well-bleached quartz and feldspar grains in these samples (i.e., those grains that indicate ages, which agreed with the expected event age within their 2-σ uncertainties: 1 year for TC Olwyn deposits at T37 and T43; 15 a for TC Vance deposit at T27) varied between 68% and 81% (T43-1), 60% (T27-1), and 31%–57% (T37-1) (Table S2). The MAM$_{bs}$ ages (Table S2) are mainly based on these grains and range from 15 ± 7 to 86 ± 11 a for quartz, from 45 ± 13 to 104 ± 40 a for IRSL, and from 100 ± 29 to 129 ± 31 a in the case of post-IRSL.

Figure 10. Comparison of quartz OSL, IRSL, and post-IRSL$_{150}$ age distributions for the TC Olwyn samples T43-1 (a) and T37-1 (b), as well as modern beach deposits T18 (c, data from Brill et al., 2017). Insets in (a) and (b) show details for the youngest grain population. The systematic shift of the peak position toward younger ages for OSL signals with higher susceptibility for signal resetting (i.e., quartz > IRSL > post-IRSL) points to OSL signal resetting during storm surge transport of the sediments. (d) Correlation of quartz remnant ages (i.e., the discrepancy between quartz OSL age and age control) and percentages of well-bleached quartz grains (percentage of grains with ages in agreement with age control within their 2-sigma uncertainties) for the modern analog samples of TC Olwyn (T43-1, T37-1) and TC Vance (T27-1). Smaller remnant ages and larger percentages of well-bleached grains point to increased OSL signal resetting prior and during transport for sediments along the central channel (T43 and T27) compared to the lateral lobes (T37). IRSL, infrared stimulated luminescence; OSL, optically stimulated luminescence; TC, tropical cyclone.
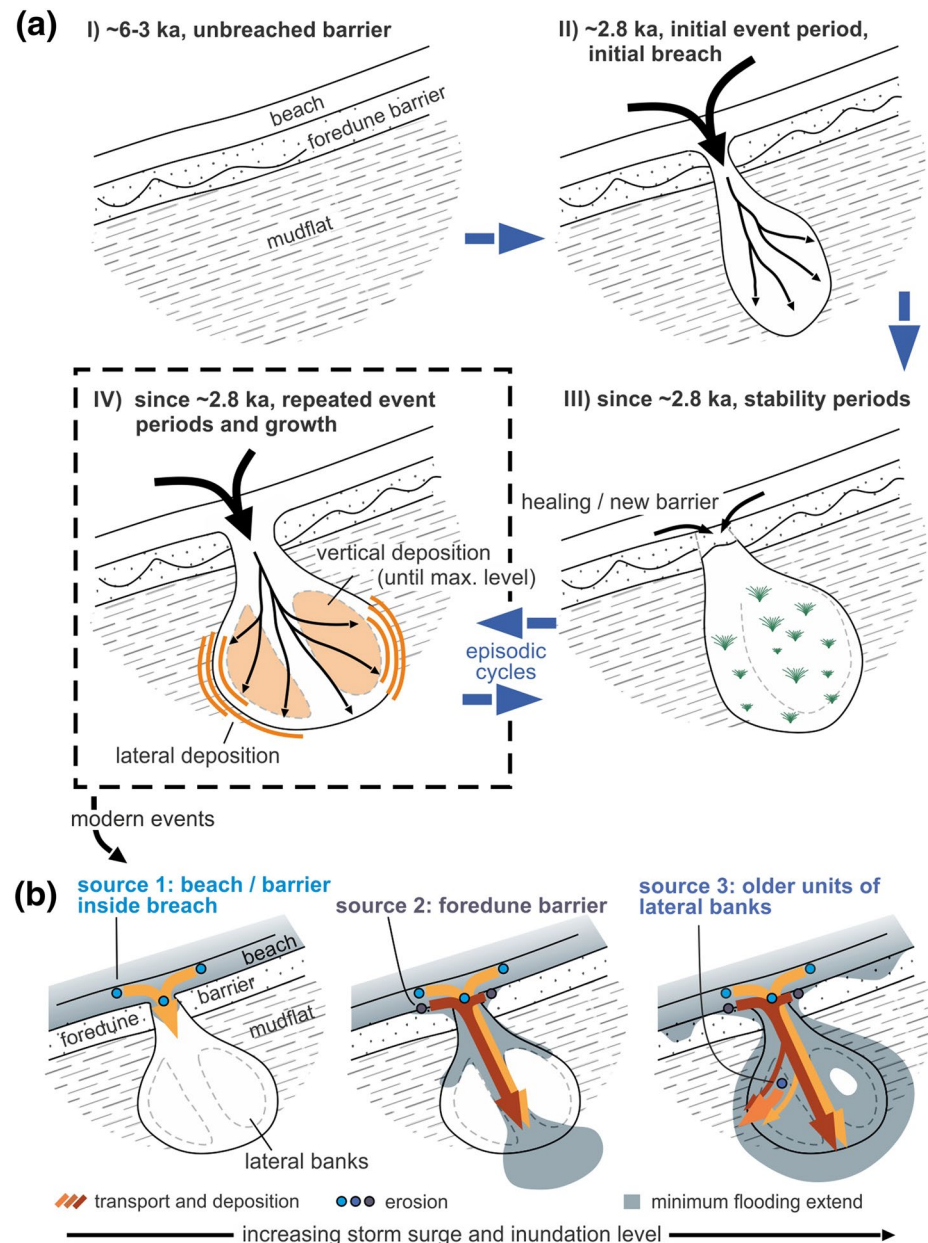
Figure 11. Schematic model of washover fan evolution as documented in this and previous studies (Brill et al., 2017, 2018; Callow et al., 2018; May et al., 2017). (a) According to the chronological results, the initial period of washover fan deposition (i.e., the deposition of the oldest units) dates to ~2,800 BP (II). Since then, repeated periods of stability (III) and episodic activity (event periods, IV) led to the vertical and lateral accretion of washover deposits, ultimately related to the growth of the washover fan. (b) Interplay between the most important sediment source environments and transport pathways as identified in this study, for different stages of the overwash event. Erosion of sediment source 3 (i.e., older washover units from the western lateral bank) can only occur when inundation levels are high enough to overtop the highest washover fan sections. Lighter/darker colors indicate sediment sources and transport pathways associated with younger/older remnant ages.

5. Discussion

5.1. Implications of Geomorphological Findings and the Deposition-Erosion Pattern

Although the accumulation of a thin sediment sheet on top of the eastern lateral bank resulted in a net sediment deposition of ~550 m^3, most significant geomorphological changes occurred in the western part of the

fan. Here, these changes were related to erosion/reworking of the western lateral bank and redistribution of sediments (washover section 14, ~450 m^3) in the form of sediment lobes along the lateral margins of the fan (Figure 4). While a clear relationship is observed between larger channels and most prominent sediment lobes, deposition occurred all along the western and southern fan margin, which must have been related to numerous smaller channels and/or sheet flow-like inundation of the lateral bank surface. Accordingly, younger (historical) TC activity in the form of thick sedimentary units was documented particularly in these western fan sections, where uppermost depositional units were luminescence-dated to 130 ± 10 a (T16) and 380 ± 30 a (T8), suggesting a distinct pattern of lateral accretion during the past ~1,300 a (Brill et al., 2017; May et al., 2017).

Sequences of millimeter- to a few centimeter-thick layers with both inverse and normal grading, horizontal bottom-set (fine to medium sand) and inclined foreset (coarse sand, shell and coral fragments) units, and an abrupt transition to the mudflat with a steep avalanching face are typical for storm-generated washover deposition (C. Donnelly et al., 2006; Paris et al., 2010; Schwartz, 1982; Shaw et al., 2015). The avalanching face with inclined sand layers, as observed at the fan's western margin, indicates subaqueous deposition and the presence of backwaters in the mudflat during the overwash event (Phantuwongraj et al., 2013; Sedgwick & Davis, 2003). Flow velocities and erosive energy of overtopping waters were highest directly behind the washover pass, as indicated by the scouring structures in the washover throat. In summary, the sedimentology and depositional pattern documented after TC Olwyn is in good agreement with deposits typically described from storm overwash elsewhere.

Our results show that erosion and deposition may be local and closely correlated. Deposition during the overwash event mostly occurred landward of fan sections that are morphologically characterized by (linear and nonlinear) erosion (Figure 4), that is, as documented for the most seaward fan sections (washover sections 1, 2, and 5, Figures 4b and 4c) or along the western (washover sections 13 and 14, Figures 4b and 4d) and southern (washover sections 7 and 8, Figures 4b and 4c) fan margins. Consequently, a general pattern of sediment redistribution and rather local sediment sources may be inferred from the geomorphological findings. This also includes a trend toward a flattening of the washover landform at several places: the uppermost ~10 cm of the pre-Olwyn surface were removed during TC Olwyn, while sediment accreted along the fan margins, ultimately contributing to the extension of the washover fan (Figures 5 and 6). This is particularly illustrated by the lateral accretion of ~450 m^3 sediment along the western margin of the fan (washover section 14, Figure 4b).

In general, our post-TC Olwyn surveys documented a pattern of deposition and erosion that corroborates the previously established model for washover fan evolution at the study site (Brill et al., 2017, 2018; Callow et al., 2018; May et al., 2017) (Figure 11a). Most of the relocated sediment seems to derive from erosion along the beach and foredune barrier (i.e., washover sections 1–3, Figure 4b), but also from local sources within the washover fan such as the lateral channels, the western lateral bank, or the southern part of the central channel (washover sections 7, 9, and 13, Figure 4b). This overall pattern of landward sediment transfer (Figure 4e) is in general accordance with barrier rollover concepts and related shifts of depositional areas (e.g., Davis & FitzGerald, 2004). In addition, the comparison of net erosion (~2,130 m^3) and deposition (~4,530 m^3) values (Figure 4f) suggest that additional sediment was transported landward into the washover system from sediment sources not captured in the DTMs, that is, the sub- to intertidal zone and/or the adjacent barrier sections.

In summary, severe TC systems traversing the Gulf (TC Vance) or passing the Gulf in direct western vicinity (TC Olwyn) from north to south (Figure 1) can cause major storm surges inside the Exmouth Gulf, related to the clockwise rotation of TC systems (Liu, 2004). Flooding of the investigated washover fan during TC Olwyn was related to inundation overwash (i.e., storm surge height equals or exceeds barrier crest elevations; J. P. Donnelly et al., 2004, 2006; cf. Orford et al., 2003), which generated sufficiently strong currents inside the washover fan for generating scour structures, dune-type bedforms, channel erosion, and deposition of sediment lobes by coarse bedload deposits. This is in accordance with a storm surge of 1 m above storm tide (i.e., ~3.2 m AHD) which was recorded at Exmouth marina during TC Olwyn (May et al., 2018) and which was capable of overtopping the pre-Olwyn barrier in the breach (~2.8 m AHD) and inundating the foredune barrier (~4 m AHD) to the west.

5.2. Sediment Dynamics Inferred From Luminescence Data

Luminescence data have a significant potential to be used as a tracer for sediment source environments and for deciphering sediment transport processes (e.g., Gray et al., 2019 and references therein). The previous investi-

gations on the Point Lefroy washover fans showed bimodal single grain quartz and feldspar age distributions for prehistoric TC deposits (Brill et al., 2017, 2018; May et al., 2017). Distinct peaks in the age distributions were interpreted to represent different sediment source environments with different pre-event remnant doses/ages. Whereas the youngest grain population of each sample was mainly interpreted as well-bleached beach sediment, the older grain populations were assumed to represent grains that were eroded from the mid-Holocene coastal barrier and/or from older depositional units of the washover fan. This would suggest a rather limited significance of bleaching during transport processes directly associated with the TC event. However, the comparison of more rapidly resetting quartz OSL signals with feldspar IRSL and post-IRSL$_{150}$ signals, the latter generally characterized by longer bleaching times (Godfrey-Smith et al., 1988), revealed a slight age increase in distinct grain populations depending on their bleaching sensitivity (Brill et al., 2018). This was interpreted as an indication for additional resetting of luminescence signals during the TC-induced sediment transport.

Based on these results, we suggest several OSL-based proxies that can be used to reconstruct the sediment dynamics during washover fan formation, and that are schematically illustrated in Figure 9. We hypothesize that (i) single grain luminescence data can be used as an indicator for the sediment source environments of TC deposits (Figures 9a and 9b) and (ii) single grain luminescence data can inform about sediment transport distance and transport mode during TCs (Figure 9c). These hypotheses shall be tested using the modern analog TC deposits of TC Olwyn (March 2015) and TC Vance (March 1999), since these deposits provide precise age control for washover deposition as well as independent information about sediment transport dynamics from drone-based change detection.

5.2.1. Source Environments of TC Deposits

Sediment sources were studied by comparing the multimodal OSL age distributions of quartz grains from the modern TC deposits with the age information (mostly quartz single grain age distributions) available for potential source environments (Figure 6). For TC Olwyn (T37-1, T43-1), pre- and post-Olwyn UAV surveying and DEMs document spatial patterns of erosion and deposition (Figures 4–6) and, thus, help in identifying possible sediment source areas (cf. Figure 6). For deposits of TC Vance (1999; T27-1), no remotely sensed data on erosion and deposition patterns are available in high resolution, but inundation during TC Vance is suggested by satellite images (Figure 1b). Since the location of trench T27 in the landward section of the washover throat seems to have been affected by deposition during TC Vance based on the satellite images, it may allow assumptions on potential source areas (Figure 2c).

In general, the pre- and post-Olwyn cross sections (Figures 4 and 5) and the pattern of erosion and deposition suggest that the active beach, the adjacent foredune barrier, the low-elevation barrier inside the breach, as well as older depositional units of the washover fan's lateral banks represent likely sediment sources. Information on their quartz OSL ages was reported by Brill et al. (2017, see Figures 6 and 9a): sediment from the active beach (T18) yielded insignificant quartz OSL remnant ages of 14 ± 2 a and nearly 100% well-bleached grains (i.e., grains yielding OSL ages in agreement with the zero age of the modern beach within their 2-sigma uncertainties). The previous studies suggested that the lateral washover fan banks are composed of deposits from at least six prehistoric TCs (or six phases of increased storminess) with ages of ~150, ~350, ~850, ~1,300, ~2,000, and ~2,800 a (e.g., T8 and T16; Brill et al., 2017; May et al., 2017). However, all events or event periods showed a rather large scatter in their single grain age distributions due to minor percentages of poorly bleached grains. In addition, the coastal foredune barrier framing the washover throat must have formed when sea level approached its mid-Holocene highstand ~6,000 a ago. Secondary barrier deposits, which have accumulated in the breached sections of the foredune barrier and now separate the washover throat from the beach (e.g., T21 in May et al., 2017; Brill et al., 2017) cannot be older than TCs which have deposited the washover deposits and should have formed within the last ~2,800 a. The pattern of erosion and deposition observed after TC Olwyn is visually coupled with the quartz OSL single grain age distributions of modern analog TC deposits and their potential source environments in Figures 6 and 9.

The landward-accreting barrier section at T43 formed during TC Olwyn (Figure 2a) by waves overwashing the pre-Olwyn barrier inside the breach, triggered by the combination of barometric and wind-driven storm surge, wave-setup, and runup. For the deposits in T43, the adjacent foredune barrier to the west and east of the breach, the pre-Olwyn barrier lying directly seawards of T43, and the adjacent modern beach are considered the only plausible sediment source environments. The youngest grain population of sample

T43-1 (P1, 0–300 a, 87% of the grains; cf. Figures 4c and 10a, Table S4) most likely represents a mixture of grains from the beach and the pre-Olwyn barrier, which was subject to repeated breaching, erosion, and/ or rebuilding during various previous historical TCs (e.g., TC Vance). Robust statistical discrimination of more specific sources within P1 is impeded by the limited precision of luminescence measurements and the single grain age scatter of some source environments (e.g., the barrier, Brill et al., 2017). Additional information on the source areas of P1 in T43-1 is provided by 68%–81% well-bleached quartz and feldspar grains (i.e., grains matching an age of 1 a within their 2-sigma errors, Table S4), which provide a maximum estimate for grains derived from the beach (i.e., the only source with complete pre-Olwyn bleaching); it cannot be excluded, however, that some of these completely bleached grains may represent sand from pre-Olwyn barrier sections, which were bleached during the very short (∼<30 m) transport path. Most of the remaining grains of T43-1 (12%) form the second grain population (P2, 500–2,000 a, Figures 4c and 10a, Table S4), which yields ages assumed to match older sections of the pre-Olwyn barrier inside the breach. Finally, only ∼1% of the sample's grains constitute P3 (4,000–6,000 a, Figure 10a and Table S4), deriving from older, non-breached foredune barrier sections, which were eroded during TC Olwyn (Figures 4–6).

T37 is representative of the prominent sediment lobes formed during TC Olwyn along the western lateral margin of the washover fan (Figures 2b, 3, and 7). As documented by the UAV-derived DEMs, this lateral accretion of sediment lobes is related to several shallow channel structures crossing the western lateral bank from east to west. Dune-type bed forms of 2.5 m wavelength indicate currents of considerable flow velocity flowing in western direction, that is, water from the inundated central channel overtopped and crossed the western lateral bank. These channels slightly shifted and incised into the underlying washover deposits during TC Olwyn, so that older depositional units from the upper part of the stratigraphy of the western lateral bank of the fan (T16 and T8 in Figure 6; May et al., 2017) represent a major sediment source for deposits in T37. Similar to T43, however, further sediment may potentially originate from the modern beach and the different barrier sections. With 45% of the grains, T37-1 is again dominated by the youngest grain population (P1, 0–300 a, 45%) (Figures 4d and 10b, Table S4), which likely represents a mixture of sediments from (i) the beach; (ii) the youngest pre-Olwyn deposits that had formed older accretionary lobes along the western bank's lateral margin (T16, 130–200 a); and (iii) both source areas mentioned before, but with a high percentage of grains bleached during transport. In agreement with that, percentages of well-bleached quartz and feldspar grains (i.e., overlapping with an expected age of 1 a within their 2-sigma uncertainties) suggest that 31%–57% of the grains in T37-1 (Table S4) were derived from the beach and/or were bleached during transport. Most of the remaining grains (P2, 300–700 a, 42%) are interpreted to originate from the uppermost stratigraphical units comprising the western bank (T8, ∼350 a; Figure 4d). Further grains (P3, 1,000–2,000 a, Figure 6, Table S4) were derived from older washover deposits found in the lower parts of the western lateral bank's stratigraphy (e.g., T8, 800–2,000 a, Figure 6, Table S4), released by local scouring and/ or lateral erosion along the central channel. The contribution of sediments from older parts of the adjacent coastal foredune barrier is again negligible.

T27 is located on top of a small sediment lobe at the distal end of the central channel (Figure 2c), which is assumed to be related to the last major flooding event before TC Olwyn, that is, TC Vance in 1999. If assuming a similar pattern of erosion and deposition during TC Vance as observed after TC Olwyn, a contribution of sediment from the beach and the low-lying barrier inside the breach is expected, similar to T43. In addition, pre-Vance deposits from the southern part of the central channel may have been reworked. This assumption is in agreement with the observation that 97% of the grains in sample T27-1 originate from grain populations with ages of 0–400 a (P1, 86%) and 500–1,000 a (P2, 11%) (Figure 4c and Table S4). A total of 60% quartz grains were well-bleached (i.e., they match an expected age of 15 a within 2-sigma errors), suggesting the beach as the dominant sediment source and/or the presence of numerous grains which were bleached during transport.

The comparison of luminescence inventories of the three modern analog TC deposits at T27, 37, and 43 points to some differences in sediment source areas, depending on the geomorphological position within the washover fan. The percentages of well-bleached grains indicate lower amounts of well-bleached sediment at T37 compared to T27 and T43 (Figure 10d and Table S4), that is, fewer grains originate from the beach and/or were bleached during transport, which may be explained as follows: At T43, indicated by the highest percentage of well-bleached grains in T43-1, waves overtopped the lowest part of the coastal barrier seaward of the washover throat and deposited beach sediments at T43 in the form of bottom-set, foreset, and top-set bed units (Fig-

ures 2–7). This may already occur during runup overwash or the overwash regime (Sallenger, 2000), but it likely continues subaqueously during the inundation regime (Figure 11b). In this area, sediment deposition rather than erosion was documented (Figures 7c and 7d; presence of pre-Olwyn soil), so older reworked sediments should be underrepresented. Since the transport path is very short as well (likely <30 m), the potential for bleaching during transport is considered limited as well. In combination, this points to the beach as the dominant source area, which predominantly yields grains already well bleached prior to storm transport.

After overtopping the barrier and inundating the washover throat, the water first spreads southwards via the main channel without significant further erosion. Particularly when the inundation regime starts, in-flowing water rapidly fills the central channel (i.e., the washover throat) and reaches ∼2.6 m AHD, that is, spill-over elevations in the central and lateral channels. Water currents are directed toward the south and follow the central channel, which is indicated by bifurcation and scouring structures (Figures 2 and 11). Here, distribution of beach sediments to the sediment lobes at the distal end of the central channel (T27) may occur, along with the erosion, scouring, transport, and redeposition of older particles from the landward part of the central channel. For this area, transport paths of deposited sand grains may be rather long compared to T43; sand particles originating from the beach must be transported for ∼450 m, and the distance for redistributed sand grains from the central channel and/or the lateral channel banks may amount up to 300 m. Located in the very landward washover section, these long transport paths may explain the rather high percentage of well-bleached grains in T27-1.

The lowest percentage of well-bleached grains was found at T37 with 31%–57% of the grains in T37-1. Deposition along the lateral margins of the washover fan's western bank is assumed to commence not before the inundation levels inside the washover throat are high enough to overtop the western lateral bank, creating incised channels crossing the bank (Figure 11b). Transport of beach sediments is considered of lower importance here, since upslope bedload transport across the lateral bank is difficult to explain, that is, mainly suspended sediment is assumed to overtop the lateral bank. The lateral accretion and the sediment lobes are to a large extent fed by sediments from the older parts of the washover fan, so that transport paths for sediment at T37 are assumed to remain below 75 m, that is, considerably lower than at T27. This interpretation of varying beach sediment contributions is also backed by larger quartz remnant ages for T37 (70 ± 12 a) compared to T43 (14 ± 7 a) and T27 (18 ± 47 a) (Figure 10d).

5.2.2. Transport Processes During Storm Inundation

Transport dynamics during storm overwash conditions were investigated by comparing the single grain age distributions of luminescence signals with different bleaching sensitivities (e.g., Reimann et al., 2015) (Figure 9c). While the peak storm surge of TC Olwyn took place at night/early morning (5 a.m.; May et al., 2018), high water levels were still observed in the morning at 8 a.m. and 11 a.m., that is, several hours after sunrise. Similar to TC Vance, bleaching of grains during transport may well have occurred. For TC Olwyn deposits at T37 and T43, the peak of the youngest grain population systematically shifts from young ages for quartz to slightly older ages for IRSL and post-IRSL$_{150}$ (Figures 10a and 10b). Since such shifts do not occur in environments with complete luminescence signal resetting such as the beach (T18, Figure 10c), and since the chronological order agrees with the bleaching sensitivities of quartz signals (highest), IRSL signals and post-IRSL signals (lowest) (Godfrey-Smith et al., 1988; Kars et al., 2014), the peak shift is interpreted as indication for the transport-related resetting of luminescence signals. Similar patterns in the luminescence inventories of storm deposits were already related to bleaching during sediment transport for older events at the study site (Brill et al., 2018).

5.3. Chronological Implications

Modern TC analogs also allow us to evaluate the luminescence dating accuracy of former studies by Brill et al. (2017, 2018), since known age samples give unambiguous insights into the remnant ages that have to be expected for local TC deposits in the various depositional environments of the washover fan. This evaluation and additional ages for pre-Olwyn and pre-Vance deposits were used to complement the existing chronological model of the washover fans given by May et al. (2017).

For the older depositional units, that is, the historical and prehistorical events inferred in May et al. (2017), it was assumed that most of the grains in the youngest grain population originate from the beach and are,

therefore, not affected by remnant ages (Brill et al., 2017, 2018). The modern analogs of TC Olwyn (T43 and T37-1) and TC Vance (T27-1) allow for an evaluation of this assumption. Quartz OSL, IRSL, and post-IRSL$_{150}$ age distributions reveal remnant ages (calculated by subtracting the event age from the luminescence age) of 14 ± 7 a (quartz), 52 ± 12 a (IRSL), and 132 ± 25 a (post-IRSL$_{150}$) for T43, 70 ± 12 a (quartz), 125 ± 38 a (IRSL), and 143 ± 31 a (post-IRSL$_{150}$) for T37-1, and 18 ± 47 a (quartz) for T27-1. Although these remnant ages are generally smaller than 150 a for all three signals, they are not in accordance with purely beach-derived sediment (T18), which revealed insignificant remnant ages for all three signals. In consequence, minor remnant ages/doses of 14–70 a or 0.01–0.06 Gy for quartz and 125–143 a or 0.15–0.20 Gy for post-IRSL$_{150}$ have to be expected in TC deposits of unknown age.

The significance of these results for the washover chronology depends on the position in the washover fan. For proximal (seaward) washover sections such as the washover throat and the barrier (i.e., T43), and for the landward part of the central channel (T27), the effects are considered low due to negligible remnant doses/ages. Assuming that most depositional units comprising the lateral banks have formed by lateral accretion—as documented for the modern analog deposits of T37 in this study, and as inferred for historical events as well (May et al., 2017)—remnant ages may indeed be of some importance for TC chronologies based on trenches from these lateral banks (i.e., T37). This is particularly true for events of historical age, where remnant ages of ∼100 a are not within the dating error. For late Holocene events, remnant ages are within luminescence dating uncertainties and therefor insignificant.

While quartz and feldspar remnant ages <150 a thus have little effect on the ages of most events incorporated in the existing chronological model of May et al. (2017), they may indeed change the interpretation of the youngest historical paleo-event (or period) inferred by these authors, dated to 130–200 years ago. However, since remnant ages depend on the position of the sampled TC deposit within the washover fan (Figure 9), a general residual correction is challenging and would require a larger data set.

In any case, the chronological model is complemented by new ages for pre-Vance deposits (T27-2) at T27 and pre-Olwyn deposits (T37-2) at T37. For sample T27-2, a quartz age of 114 ± 36 a suggests deposition during the youngest (historical) paleo-event given in May et al. (2017); the age of the overlying TC Vance deposits in the same trench is ∼90 a younger (T27-1). For the pre-Olwyn TC sediments at T37 (sample T37-2), quartz and feldspar ages (86 ± 11 a) are hardly distinguishable from the ages of the TC Olwyn deposits (71 ± 12 a) at the same site. Considering the high remnant ages at this site, these results point to the formation of the pre-Olwyn sand sheet by TC Vance in 1999, which generally agrees with the inferred inundation of the washover fan based on satellite images (Figure 1).

6. Conclusions

Based on pre- and post-TC surveys, the application of UAV- and photogrammetry techniques, luminescence dating, and the use of luminescence-based proxies for sediment dynamics, this study investigated the impact of TC Olwyn on a large washover fan in NW Australia (Exmouth Gulf). High-resolution pre- and post-TC Olwyn DEMs resulted in a detailed image of deposition and erosion, providing information on hydrodynamics, source areas of redeposited sediments, inundation limits, and the most important depositional processes during the event.

Single grain luminescence data helped to reconstruct sediment source areas and transport distances of the washover deposits, which differ depending on their position within the washover fan. Washover deposits behind the barrier and along the central channel seem to consist of well-bleached deposits due to the beach being the dominant source area and/or comparatively long transport distances. Lateral washover fan positions, in contrast, receive their sediment from rather local source areas represented by older washover deposits that were transported over short distances.

Related to these differences in sediment sources and transport pathways, remnant ages may considerably differ depending on washover position. Higher remnant ages of 70–140 a (in the case of this washover fan) can be expected for sites where reworking of older washover units occurs and/or sediment pathways are short, that is, particularly related to the landward accretion of the lateral banks. These results indicate that local chronologies

may be biased for events younger than a few centuries and demand a careful consideration of local processes and source areas when establishing sediment-based chronologies of past TCs or other coastal processes.

This study clearly points to the potential of luminescence data (i.e., luminescence inventories) for investigating the formation of deposits of extreme-wave events such as TCs and tsunamis. Although this study is based on a small number of samples—we suggest that future studies follow a more systematic sampling approach—the outcomes demonstrate the significance of luminescence data in palaeotempestology beyond its use as a chronometer.

Finally, the combination of single grain luminescence data and drone-derived high-resolution data on geomorphological changes is applicable to a wide range of geomorphological systems worldwide. As documented in this study, this approach has the potential (i) to quantify the complex interplay of erosion and deposition; (ii) to decipher sediment source environments; and (iii) to reconstruct sediment transport pathways and processes on very high temporal and spatial scales, thereby ultimately contributing to a better understanding of the evolution of numerous event-driven depositional landforms in general.

Data Availability Statement

Drone-derived data sets can be accessed via the data repository of the University of Western Australia (Callow, 2020; DOI: https://doi.org/10.26182/m4de-b822).

References

Arnold, L. J., & Roberts, R. G. (2009). Stochastic modelling of multi-grain equivalent dose (De) distributions: Implications for OSL dating of sediment mixtures. *Quaternary Geochronology*, *4*. 204–230.

Auclair, M., Lamothe, M., & Huot, S. (2003). Measurement of anomalous fading for feldspar IRSL using SAR. *Radiation measurements*, *37*(4-5), 487–492.

Bureau of Meteorology (BoM). (2016a). *Climate statistics for Australian locations—Station 005007 (Learmonth Airport)*. Retrieved from http://www.bom.gov.au/climate/averages/tab-les/cw_005007.shtml

Bureau of Meteorology (BoM). (2016b). *Tropical cyclones affecting Exmouth*. Retrieved from http://www.bom.gov.au/cyclone/history/wa/ons-low.shtml

Bureau of Meteorology (BoM). (2016c). *Tropical cyclone Vance, official report of the Bureau of Meteorology*. Retrieved from http://www.bom.gov.au/cyclone/history/pdf/vance.pdf

Brill, D., Klasen, N., Brückner, H., Jankaew, K., Kelletat, D., Scheffers, A., & Scheffers, S. (2012). Local inundation distances and regional tsunami recurrence in the Indian Ocean inferred from luminescence dating of sandy deposits in Thailand. *Natural Hazards and Earth System Sciences*, *12*, 2177–2192.

Brill, D., Klasen, N., Brückner, H., Jankaew, K., Scheffers, A., Kelletat, D., & Scheffers, S. (2012). OSL dating of tsunami deposits from Phra Thong Island, Thailand. *Quaternary Geochronology*, *10*, 224–229.

Brill, D., May, S. M., Shah-Hosseini, M., Rufer, D., Schmidt, C., & Engel, M. (2017). Luminescence dating of cyclone-induced washover fans at Point Lefroy (NW Australia)—Establishing chronologies for heterogeneous and discontinuous sediment archives. *Quaternary Geochronology*, *41*, 134–150.

Brill, D., Reimann, T., Wallinga, J., May, S. M., Engel, M., Riedesel, S., & Brückner, H. (2018). Testing the accuracy of feldspar single grains to date late Holocene cyclone and tsunami deposits. *Quaternary Geochronology*, *48*, 91–103.

Callow, J. N. (2020). *Revealing sediment transport pathways and geomorphic change in washover fans by combining drone-derived digital elevation models and single grain luminescence data*. The University of Western Australia. https://doi.org/10.26182/m4de-b822

Callow, J. N., May, S. M., & Leopold, M. (2018). Drone photogrammetry and KMeans point cloud filtering to create high resolution topographic and inundation models of coastal sediment archives. *Earth Surface Processes and Landforms*, *43*, 2603–2615.

Chamberlain, E. L., Wallinga, J., & Shen, Z. (2018). Luminescence age modeling of variably bleached sediment: Model selection and input. *Radiation Measurements*, *120*, 221–227.

Chand, S. S., Tory, K. J., McBride, J. L., Wheeler, M. C., Dare, R., & Walsh, K. J. E. (2013). The different impact of positive-neutral and negative-neutral ENSO regimes on Australian tropical cyclones. *Journal of Climate*, *26*, 8008–8016.

Collins, L. B., Zhu, Z. R., Wyrwoll, K.-H., & Eisenhauer, A. (2003). Late Quaternary structure and development of the northern Ningaloo Reef, Australia. *Sedimentary Geology*, *159*, 81–94.

Cunningham, A., & Wallinga, J. (2012). Realizing the potential of fluvial archives using robust OSL chronologies. *Quaternary Geochronology*, *12*, 98–106.

Davids, F., Duller, G. A. T., & Roberts, H. M. (2010). Testing the use of feldspars for optical dating of hurricane overwash deposits. *Quaternary Geochronology*, *5*, 125e130.

Davis, R. A., & FitzGerald, D. M. (2004). *Beaches and coasts*. Oxford, England: Blackwell.

Denniston, R. F., Villarini, G., Gonzales, A. N., Wyrwoll, K.-H., Polyak, V. J., Ummenhofer, C. C., et al. (2015). Extreme rainfall activity in the Australian tropics reflects changes in the El Niño/Southern Oscillation over the last two millennia. *Proceedings of the National Academy of Sciences of the United States of America*, *112*(15), 4576–4581.

Donnelly, J. P., Butler, J., Roll, S., Wengren, M., & Webb, T. (2004). A backbarrier overwash record of intense storms from Brigantine, New Jersey. *Marine Geology*, *210*, 107–121.

Donnelly, C., Kraus, N., & Larson, M. (2006). State of knowledge on measurement and modeling of coastal overwash. *Journal of Coastal Research*, *22*, 965–991.

Durcan, J. A., King, G. E., & Duller, G. A. (2015). DRAC: Dose Rate and Age Calculator for trapped charge dating. *Quaternary Geochronology*, *28*, 54–61.

Eliot, I., Gozzard, J. R., Eliot, M., Stul, T., & McCormack, G. (2012). *The coast of the shires of Shark Bay to Exmouth, Gascoyne, Western Australia: Geology, geomorphology & vulnerability*. Prepared by Damara WA Pty. Ltd. and Geological Survey of Western Australia for the Department of Planning and the Department of Transport. Retrieved from http://www.transport.wa.gov.au/mediaFiles/marine/MAC_R_ShiresOfSharkBayAndExmouthFullReport.pdf

Emanuel, K. (2005). Increasing destructiveness of tropical cyclones over the past 30 years. *Nature*, *436*, 686–688.

Forsyth, A. J., Nott, J., & Bateman, M. D. (2010). Beach ridge plain evidence of a variable late-Holocene tropical cyclone climate, North Queensland, Australia. *Palaeogeography, Palaeoclimatology, Palaeoecology*, *297*(3–4), 707–716.

Galbraith, R. F., & Roberts, R. G. (2012). Statistical aspects of equivalent dose and error calculation and display in OSL dating: An overview and some recommendations. *Quaternary Geochronology*, *11*, 1–27.

Godfrey-Smith, D. I., Huntley, D. J., & Chen, W. H. (1988). Optical dating studies of quartz and feldspar sediment extracts. *Quaternary Science Reviews*, *7*, 373–380.

Gray, H., Jain, M., Sawakuchi, A. O., Mahan, S. A., & Tucker, G. E. (2019). Luminescence as a sediment tracer and provenance tool. *Reviews of Geophysics*, *57*, 987–1017.

Huntley, D. J., & Lamothe, M. (2001). Ubiquity of anomalous fading in K-feldspars and the measurement and correction for it in optical dating. *Canadian Journal of Earth Sciences*, *38*, 1093–1106.

James, M. R., Robson, S., d'Oleire-Oltmanns, S., & Niethammer, U. (2017). Optimising UAV topographic surveys processed with structure-from-motion: Ground control quality, quantity and bundle adjustment. *Geomorphology*, *280*, 51–66.

Joint Typhoon Warning Center (JTWC). (2016). *Southern Hemisphere best track data*. Retrieved from https://metoc.ndbc.noaa.gov/web/guest/jtwc/best_tracks/southern-hemisphere

Kars, R., Reimann, T., Ankjærgaard, C., & Wallinga, J. (2014). Bleaching of the post-IR IRSL signal: New insights for feldspar luminescence dating. *Boreas*, *43*, 780–791.

Kuleshov, Y., Qi, L., Fawcett, R., & Jones, D. (2008). On tropical cyclone activity in the Southern Hemisphere: Trends and the ENSO connection. *Geophysical Research Letters*, *35*, L14S08. https://doi.org/10.1029/2007GL032983

Kunz, A., Frechen, M., Ramesh, R., & Urban, B. (2010). Revealing the coastal event history of the Andaman Islands (Bay of Bengal) during the Holocene using radiocarbon and OSL dating. *International Journal of Earth Sciences*, *99*, 1741–1761.

Lambeck, K., & Nakada, M. (1990). Late Pleistocene and Holocene sea-level change along the Australian coast. *Palaeogeography, Palaeoclimatology, Palaeoecology*, *89*, 143–176.

Lazarus, E. D., & Armstrong, S. (2015). Self-organized pattern formation in coastal barrier washover deposits. *Geology*, *43*(4), 363–366.

Lewis, S. E., Sloss, C. R., Murray-Wallace, C. V., Woodroffe, C. D., & Smithers, S. G. (2013). Post-glacial sea-level changes around the Australian margin: A review. *Quaternary Science Reviews*, *74*, 115–138.

Liu, K.-b. (2004). Palaeotempestology: Principles, methods, and examples from Gulf Coast lake sediments. In R. J. Murnane, & K.-b. Liu (Eds.), *Hurricanes and typhoons. Past, present, and future* (pp. 13–57). New York, NY: Columbia University Press.

Lough, J. M. (1998). Coastal climate of northwest Australia and comparisons with the Great Barrier Reef: 1960 to 1992. *Coral Reefs*, *17*, 351–367.

Matias, A., Ferreira, Ó., Vila-Concejo, A., Morris, B., & Dias, J. A. (2010). Short-term morphodynamics of non-storm overwash. *Marine Geology*, *274*, 69–84.

Matias, A., Ferreira, Ó., Vila-Concejo, A., Garcia, T., & Dias, J. A. (2008). Classification of washover dynamics in barrier islands. *Geomorphology*, *97*, 655–674.

May, S. M., Brill, D., Engel, M., Scheffers, A., Pint, A., Opitz, S., et al. (2015). Traces of historical tropical cyclones and tsunamis in the Ashburton Delta (NW Australia). *Sedimentology*, *62*, 1546–1572.

May, S. M., Brill, D., Leopold, M., Callow, J. N., Engel, M., Scheffers, A., et al. (2017). Chronostratigraphy and geomorphology of washover fans in the Exmouth gulf (NW Australia)—A record of tropical cyclone activity during the late Holocene. *Quaternary Science Reviews*, *169*, 65–84.

May, S. M., Gelhausen, H., Brill, D., Callow, J. N., Engel, M., Scheffers, A., et al. (2018). Chenier-type ridges in Giralia Bay (Exmouth Gulf, Western Australia)—Processes, chronostratigraphy, and significance for recording past tropical cyclones. *Marine Geology*, *396*, 186–204.

McCall, R. T., Van Thiel de Vries, J. S. M., Plant, N. G., Van Dongeren, A. R., Roelvink, J. A., Thompson, D. M., & Reniers, A. J. H. M. (2010). Two-dimensional time dependent hurricane overwash and erosion modeling at Santa Rosa Island. *Coastal Engineering*, *57*(7), 668–683.

Murray, A.S., & Wintle, A.G. (2003). The single aliquot regenerative dose protocol: potential for improvements in reliability. *Radiation Measurements*, *37*, 377e381.

Morton, R. A., & Sallenger, A. H. (2003). Morphological impacts of extreme storms on sandy beaches and barriers. *Journal of Coastal Research*, *19*(3), 560–573. https://doi.org/10.2307/4299198

Nicholls, N. (1984). The Southern Oscillation, sea-surface-temperature, and interannual fluctuations in Australian tropical cyclone activity. *Journal of Climatology*, *4*, 661–670.

Nott, J. (2011). A 6000-year tropical cyclone record from Western Australia. *Quaternary Science Reviews*, *30*, 713–722.

Nott, J., & Hubbert, G. (2005). Comparisons between topographically surveyed debris lines and modelled inundation levels from severe tropical cyclones *Vance* and *Chris*, and their geomorphic impact on the sand coast. *Australian Meteorological Magazine*, *54*, 187–196.

Nott, J., Smithers, S., Walsh, K., & Rhodes, E. (2009). Sand beach ridges record 6000-year history of extreme tropical cyclone activity in northeastern Australia. *Quaternary Science Reviews*, *28*, 1511–1520.

Orford, J. D., Murdy, J. M., & Wintle, A. G. (2003). Prograded Holocene beach ridges with superimposed dunes in north-east Ireland: Mechanisms and timescales of fine and coarse beach sediment decoupling and deposition. *Marine Geology*, *194*, 47–64.

Orpin, A. R., Haig, D. W., & Woolfe, K. J. (1999). Sedimentary and foraminiferal facies in Exmouth Gulf, in arid tropical northwestern Australia. *Australian Journal of Earth Sciences*, *46*, 607–621.

Paris, R., Fournier, J., Poizot, E., Etienne, S., Morin, J., Lavigne, F., & Wassmer, P. (2010). Boulder and fine sediment transport and deposition by the 2004 tsunami in Lhok Nga (western Banda Aceh, Sumatra, Indonesia): A coupled offshore-onshore model. *Marine Geology*, *268*, 43–54.

Phantuwongraj, S., Choowong, M., Nanayama, F., Hisada, K. I., Charusiri, P., Chutakositkanon, V., et al. (2013). Coastal geomorphic conditions and styles of storm surge washover deposits from Southern Thailand. *Geomorphology*, *192*, 43–58.

Priestas, A. M., & Fagherazzi, S. (2010). Morphological barrier island changes and recovery of dunes after Hurricane Dennis, St. George Island, Florida. *Geomorphology*, *114*, 614–626. https://doi.org/10.1016/j.geomorph.2009.09.022

Reimann, T., Notenboom, P. D., De Schipper, M. A., & Wallinga, J. (2015). Testing for sufficient signal resetting during sediment transport using a polymineral multiple-signal luminescence approach. *Quaternary Geochronology*, *25*, 26–36.

Sallenger, A. H. (2000). Storm impact scale for barrier islands. *Journal of Coastal Research*, *16*, 890–895.

Scheffers, S. R., Scheffers, A., Kelletat, D., & Bryant, E. A. (2008). The Holocene paleo-tsunami history of West Australia. *Earth and Planetary Science Letters*, *270*, 137–146.

Schwartz, R. K. (1982). Bedform and stratification characteristics of some modern small-scale washover sand bodies. *Sedimentology*, *29*, 835–849.

Sedgwick, P. E., & Davis, R. A. (2003). Stratigraphy of washover deposits in Florida: Implications for recognition in the stratigraphic record. *Marine Geology*, *200*, 31–48.

Semeniuk, V. (1996). Coastal forms and Quaternary processes along the arid Pilbara coast of northwestern Australia. *Palaeogeography, Palaeoclimatology, Palaeoecology*, *123*, 49–84.

Shaw, J., You, Y., Mohrig, D., & Kocurek, G. (2015). Tracking hurricane-generated storm surge with washover fan stratigraphy. *Geology*, *43*, 127–130.

Short, A. D. (2005). *Beaches of the Western Australian coast: Eucla to Roebuck Bay*. Sydney, Australia: Sydney University Press.

Short, A. D., & Woodroffe, C. D. (2009). *The coast of Australia*. Cambridge, England: Cambridge University Press.

Smedley, R. K., Duller, G. A. T., Pearce, N. J. G., & Roberts, H. M. (2012). Determining the K-content of single-grains of feldspar for luminescence dating. *Radiation Measurements*, *47*, 790–796.

Tamura, T., Oliver, T. S. N., Cunningham, A. C., & Woodroffe, C. D. (2019). Recurrence of extreme coastal erosion in SE Australia beyond historical timescales inferred from beach ridge morphostratigraphy. *Geophysical Research Letters*, *46*(9), 4705–4714. https://doi.org/10.1029/2019GL083061

Wheaton, J. M., Brasington, J., Darby, S. E., & Sear, D. A. (2010). Accounting for uncertainty in DEMs from repeat topographic surveys: Improved sediment budgets. *Earth Surface Processes and Landforms*, *35*, 136–156.

White, S. A., & Wang, Y. (2003). Utilizing DEMs derived from LIDAR data to analyze morphologic change in the North Carolina coastline. *Remote Sensing of Environment*, *85*, 39–47. https://doi.org/10.1016/S0034-4257(02)00185-2

Wyrwoll, K.-H., Kendrick, G., & Long, J. A. (1993). The geomorphology and late Cenozoic geomorphological evolution of the Cape Range–Exmouth Gulf Region. In W. F. Humphreys (Ed.), *The biogeography of cape range, Western Australia* Vol. (*45*, pp. 1–23). Welshpool, Western Australia: Records of the Western Australian Museum.